PCCP

Rotational-vibrational resonance states

SCHOLARONE™
Manuscripts

Journal Name

ARTICLE TYPE

Rotational-vibrational resonance states

Attila G. Császár,[*a,b] Irén Simkó[b], Tamás Szidarovszky[*b,c], Gerrit C. Groenenboom[d], Tijs Karman[e], and Ad van der Avoird[*d]

Resonance states are characterized by an energy that is above the lowest dissociation threshold of the potential energy hypersurface of the system and thus resonances have finite lifetimes. All molecules possess a large number of long- and short-lived resonance (quasibound) states. A considerable number of rotational-vibrational resonance states are accessible not only *via* quantum-chemical computations but also by spectroscopic and scattering experiments. In a number of chemical applications, most prominently in spectroscopy and reaction dynamics, consideration of rotational-vibrational resonance states is becoming more and more common. There are different first-principles techniques to compute and rationalize rotational-vibrational resonance states: one can perform scattering calculations or one can arrive at rovibrational resonances using variational or variational-like techniques based on methods developed for determining bound eigenstates. The latter approaches can be based either on the Hermitian (L^2, square integrable) or non-Hermitian (non-L^2) formalisms of quantum mechanics. This Perspective reviews the basic concepts related to and the relevance of shape and Feshbach-type rotational-vibrational resonance states, discusses theoretical methods and computational tools allowing their efficient determination, and shows numerical examples from the authors' previous studies on the identification and characterization of rotational-vibrational resonances of polyatomic molecular systems.

1 Introduction

The quantum phenomenon of resonances,[1–6] *i.e.*, the existence of metastable (quasibound) states embedded in the continuum spectra of Hamiltonians, plays an important, often crucial role in a number of fields related to atomic and molecular physics and chemistry. These include the process of α decay (where resonance states were perhaps first considered in 1928),[1] nuclear reactions,[7,8] binary elementary reactions,[4,5,9–11] high-resolution molecular spectroscopy,[12–14] transition-state spectroscopy,[15–17] unimolecular decomposition,[18] (reactive) scattering (the first scattering resonance in atoms was observed in 1963[19]),[19–21] electronic,[22] vibrational,[23,24] and rotational[25] predissociation, autoionization,[26] photoionization,[27] photodissociation,[28,29] photoassociation[30] and magnetoassociation,[31] con-

trolled cold and ultracold chemistry,[32–34] and the list could be easily continued. In this perspective we focus on the rotational-vibrational resonances of polyatomic molecules, playing a fundamental role in chemical reactions, as well as in molecular scattering and spectroscopy. Although resonance states of a system have higher energy than a corresponding dissociation limit (most often the first one, but this may not always be the case, *vide infra*), dissociation from these states does not happen instantaneously.

Resonance states have well-defined finite lifetimes, which can be very short or very long, to some extent independent of the energy of the state. One must thus emphasize that despite their somewhat unusual properties, resonance states are always "genuine", they arise from intrinsic properties characterizing most quantum systems. Thus, rotational-vibrational (rovibrational) resonance states should be considered neither exotic nor esoteric,[35] as both their experimental observation[10,12,16,17,35–55] and first-principles characterization[13,14,47,56–68] is becoming increasingly feasible. Rovibrational resonances are especially important for scattering events and for spectroscopic observations at energies exceeding that of the lowest dissociation limit.

In quantum mechanics (QM) the states, the associated energies, and the time evolution of quantum systems are defined by appropriately chosen Hamiltonians, $\hat{H}$. In standard QM[69–71] it is usual to argue that the Hamiltonians describing molecular systems are Hermitian operators. This choice is made in order to

[a] *MTA-ELTE Complex Chemical Systems Research Group, P.O. Box 32, H-1518 Budapest 112, Hungary; E-mail: csaszarag@caesar.elte.hu*

[b] *Institute of Chemistry, ELTE Eötvös Loránd University, H-1117 Budapest, Pázmány Péter sétány 1/A, Hungary*

[c] *MTA-ELTE Complex Chemical Systems Research Group, P.O. Box 32, H-1518 Budapest 112, Hungary; E-mail: tamas821@caesar.elte.hu*

[d] *Institute of Theoretical Chemistry, Institute for Molecules and Materials, Radboud University, Heyendaalseweg 135, 6525 AJ, Nijmegen, Netherlands; E-mail: A.vanderAvoird@theochem.ru.nl*

[e] *Center for Astrophysics, Harvard & Smithsonian, 60 Garden Street, Cambridge, MA 02138, USA*

guarantee that the eigenspectrum of $\hat{H}$ is real and the time evolution of the molecular system is unitary. However, Hermiticity of an operator does not depend solely on the form of the operator itself but also on the functions we let it operate on. In standard, Hermitian QM (HQM), $\hat{H}$ acts upon functions in the L^2 Hilbert space[71] and this is equivalent to stating that the boundary conditions are such that the functions must vanish at infinity. This boundary condition is suitable to describe bound states, but not applicable for those states which lie above the dissociation energy of the system, *i.e.*, resonance states and the scattering continuum, because their wave functions can have nonzero values at infinity. In the time-independent HQM approach to scattering the continuum can be associated with bounded, Dirac-normalizable functions, and this can be directly linked[20] with the motion of square-integrable wave packets in a time-dependent picture.

There is another branch of QM, non-Hermitian quantum mechanics (NHQM),[72,73] where the functions upon which $\hat{H}$ is allowed to act have different boundary conditions.[74] We are only interested in those cases where these functions are suitable to represent rovibrational resonance states. Note that a Hamiltonian that acts on square-integrable functions but contains a complex potential, appearing in some resonance-computing techniques, is also non-Hermitian, leading to NHQM. NHQM as well as the theory of resonances has a rather complex mathematical background. A rigorous mathematical theory of resonance states has been formulated.[75,76] Nevertheless, intuitive approaches aiming at the understanding of the quantum phenomenon of resonances are also available, leading to useful tools for a variety of practical applications. We are going to follow the intuitive route in this Perspective.

In the Schrödinger representation of NHQM, resonance states can be associated[69,77] with those eigenfunctions of the Hamiltonian which have an outgoing boundary condition and diverge exponentially at infinity, as detailed below. Due to the non-L^2 nature of these eigenstates, the Hermiticity of the Hamiltonian is lost and the resonances are characterized by complex eigenvalues. The complex resonance eigenvalues are usually written, in atomic units (utilized from here on), as

$$E_n^{\text{res}} = \varepsilon_n - \frac{\text{i}}{2}\Gamma_n, \tag{1}$$

where $\varepsilon_n = \text{Re}(E_n^{\text{res}})$ is the resonance position (with respect to the (real) ground-state energy of the system), i is the imaginary unit, and $\Gamma_n \propto \text{Im}(E_n^{\text{res}})$ is the full width at half maximum (FWHM) of the resonance state, related to the inverse lifetime by

$$P_n(\mathbf{q},t) \propto e^{-\Gamma_n t}, \tag{2}$$

where $P_n(\mathbf{q},t)$ is the probability density of finding the quantum system at a given $\mathbf{q}$ point in coordinate space at time t.

For most physicists resonances are understood as part of scattering theory. Let us call this a top-down approach to resonances as we approach the dissociation limit, and the underlying bound states, from above. From the scattering, top-down point of view, resonances occur when molecules collide with a certain energy and form a long-lived collision complex before they fly apart. The

colliding molecules have more time to interact and if one monitors the outcome of a scattering event —quantified by the scattering cross sections as a function of the collision energy— one can observe that these are very different at resonance energies than otherwise. When studying resonances by scattering computations, the resonant contributions to the cross sections must be separated from the smooth background caused by the usual scattering states. The most common top-down (scattering) technique is the coupled-channels method,[20] but the Kohn variational method[78–81] is also very useful to compute and characterize resonances. An alternative approach to this is a bottom-up one, in which resonances are considered as a continuation of bound states into the continuum. In the case of rovibrational resonances the top-down (scattering) and the bottom-up (spectroscopic) approaches are complementary to each other. In both the spectroscopic and scattering approaches one relies on the total rotational quantum number J as a good quantum number, but in scattering theory the observable quantities refer to the asymptotically correct rotational quantum numbers j of the interacting partners, and have to be calculated by inclusion of the results obtained for all J values.

Because the wave functions of resonance states are not square integrable, the techniques employed during the variational solution of the time-independent nuclear Schrödinger equation (TInSE) of bound states, resulting in square-integrable wave functions,[82,83] need to be modified for the computation of resonance states. The most common bottom-up approaches to compute rovibrational resonance states are the stabilization method (SM),[84–87] the complex absorbing potential (CAP) method,[88,89] and the complex coordinate scaling (CCS) method (also referred to as the method of dilatation analytic continuation).[90–98] Determination of rovibrational resonance states using any of these techniques is not nearly as advanced as that of bound states. Nevertheless, the field of first-principles computation of rovibrational resonances matured considerably during the last decade and it is now possible to compute a large number of rovibrational resonances for real polyatomic systems and compare them with their experimental counterparts. This Perspective deals with the field of first-principles, bottom-up and top-down computation of rotational-vibrational resonance states, emphasising on how the authors see it, without attempting to provide a thorough review of all related developments and results from other laboratories.

The first-principles computation of rovibrational resonance states may utilize several sophisticated Hermitian and non-Hermitian techniques of molecular scattering and variational nuclear-motion theories. Whatever is the choice of the Hamiltonian, computation and characterization of rovibrational resonance states offer several notable challenges: (a) The potential energy surfaces (PES) employed for rovibrational resonance computations must have correct asymptotic behavior. Quantum-chemical scattering computations repeatedly indicate[48,99] that the resonance characteristics strongly depend on the topology of the PES. It is not straightforward to ensure the correct asymptotics during the generation and the fitting of reactive PESs and most PESs in the literature in fact do not obey this criterion. (b) Usually large basis sets need to be employed, at one stage or another,

during variational (or variational-like) resonance-state computations to ensure convergence of the computed states. This makes resonance-state computations relatively computer intensive. (c) Usually molecules possess a large number of bound states below the resonance states and the explicit consideration of bound states may increase substantially the cost of resonance-state computations of larger polyatomic systems. (d) Due to heavy mixing of the states, it is rarely transparent how to characterize the computed resonances and provide reasonable, physically-motivated meaning for them. (e) Since resonances have vastly different lifetimes, it is not straightforward to ensure that all resonances are computed within a particular setup of the nuclear-motion or scattering computation correctly. In fact, one of the biggest challenges in this field is the computation of converged lifetimes of rovibrational resonances.

Among the several possible bottom-up variational approaches[77,100] for computing quasibound (ro)vibrational states and understanding near-dissociation high-resolution molecular spectra, some require the computation of all the bound states of the molecule, as well. For polyatomic molecules this task often requires a substantial amount of work both via electronic-structure and nuclear-motion computations,[83] and the amount of effort needed strongly depends on the specific system investigated. Especially within their ground electronic state, most polyatomic molecular systems have a very large number of bound rovibrational states. For example, the isotopomers of the triatomic water molecule possess rovibrational states on the order of a million below the first dissociation limit,[101,102] about 40 000 cm^{-1}.[42] In the fourth age of quantum chemistry[83] sophisticated variational and variational-like techniques have been developed[82,83,103] for solving the TInSE, which allows the characterization of all bound states of a molecule.[101,102] These advanced numerical computations require a large amount of computer time. Nevertheless, once the computations are set up properly, very little human intervention is needed. These studies revealed extremely rich and complex nuclear dynamics for the bound states of molecular systems, especially close to the dissociation limit(s).[104,105] Occasionally the complexity of the motions increases to the extent that the rotational and vibrational motions cannot be separated any more. This may happen even for the lowest-energy states, leading to quasistructural molecular systems,[106] like H_5^+,[107–109] CH_5^+,[110,111] and the $CH_4 \cdot H_2O$ dimer.[112,113] In the case of weakly-bound complexes, having a dissociation energy smaller than that of typical stretch or bend fundamentals, resonance states are formed straightforwardly by the excitation of a vibrational mode in one of the monomers. Experimental techniques, like predissociation spectroscopy,[24,114,115] take full advantage of the existence of resonance states.

Numerical simulations have demonstrated that molecular systems can exhibit a considerable number of rovibrational resonance states with energies even well above their first dissociation limit. For example, the $Ar \cdot NO^+$ cationic complex was shown to have a large number of long-lived vibrational resonances even at 8000 cm^{-1}, nine times its dissociation energy, $D_0 = 887$ cm^{-1}.[64] Beyond theoretical investigations, spectroscopic access to resonance states is often straightforward due to their considerable

lifetime. In the case of molecular complexes, the long lifetimes are the consequence of the adiabatic separation of the dissociative motion from the rest of the nuclear motions (the separation is almost perfect for $Ar \cdot NO^+$, explaining the long lifetimes computed up to 8000 cm^{-1}).

A large amount of direct information about rotational-vibrational resonances can be obtained from scattering experiments, as well. State-to-state scattering cross sections, both differential (DCS) and integral (ICS), are measured in considerable detail in crossed-molecular-beam experiments. Early observations of resonances in such experiments on H-Hg are described by Scoles et al.[36,37] and on the H-Ar, H-Kr, H-Xe, H_2-Ar, H_2-Kr, and H_2-Xe systems by Toennies et al.[38–40] Recently, new experiments with the possibility to scan the collision energy with sufficiently high resolution to detect even narrow resonances and access the low-energy region where most resonances are expected, made it possible to study resonances in more detail. Resonances in rate coefficients determined by the ICSs for Penning ionization processes were found by Narevicius et al.[45,46,51] and by Osterwalder et al.[52,53] in a merged-beam approach, with collision temperatures down to the millikelvin (mK) regime. Using cryogenically cooled beams of CO and O_2 crossed with beams of He or H_2 at a variable angle, resonances in the state-to-state ICSs for rotationally inelastic collisions with energies down to 4 cm^{-1} were observed by Costes et al.[43,44,49] By controlling the velocity of the molecules in one of the beams with a Stark decelerator, reducing the angle between the beams to 5°, and combining the crossed-beam setup with velocity map imaging (VMI), Van de Meerakker et al.[47,66,116] made it possible not only to observe resonance peaks in ICSs at collision energies down to 0.2 cm^{-1} but also to measure the corresponding DCSs with a resolution of about 1°, such that even the narrow diffraction oscillations are well resolved. Another promising technique to observe resonances in collisions of vibrationally and rotationally excited molecules is the use of co-axial beams, as developed by Suits et al.[54,55] The recent experiments were accompanied by theoretical studies of resonances in molecule-molecule scattering based on high-quality ab initio intermolecular potential surfaces and the QM coupled-channels or close-coupling (CC) approach.

Long-lived complexes formed during resonant collisions are of special interest in the ultracold regime,[32,34,117,118] defined by translational temperatures, usually below 1 mK, where consideration of a single partial wave is sufficient. As the temperature drops below 1 μK, the collision energy essentially vanishes; thus, resonances do not occur by matching the collision energy to a resonance state but rather by tuning the energy of a resonance state across the dissociation limit. Such tuning of a resonance state relative to the lowest threshold can be achieved, for example, by using an external magnetic field. As a resonance state is tuned across threshold it becomes a bound state. By performing this sweep adiabatically it is possible to populate this bound state. This process is called magnetoassociation[31] and enables the formation of weakly bound molecules from ultracold atoms.[119,120] Another application of resonances in ultracold gases is to control interactions.[117,118] As one tunes a resonance state across threshold the scattering phase shift jumps by π and the scattering length

scans through all values between $-\infty$ and $+\infty$. This scattering length determines the pseudo-potential that governs the interactions between ultracold atoms or molecules, and its external field control using resonances has opened up the field of quantum simulation, [118,121–124] and enabled the study of novel quantum phases of matter. [125–130]

Quantum chemical studies of resonances in ultracold gases are difficult, especially for heavier nuclei where the density of resonances becomes very high. [131] This is illustrated by recent CC calculations [132] on K$_2$-Rb scattering; even with specially developed methods they required enormous computational effort. This study not only identified an extensive set of resonances, but also showed that the positions and widths of these resonances are in good agreement with the Wigner–Dyson [133,134] and Porter–Thomas [135] distributions associated with quantum chaos.

The remainder of this Perspective is structured as follows. The theory of quasibound states, including discussion of several elementary models, is reviewed in Section 2. Then potential energy hypersurfaces employed for rotational-vibrational resonance computations are discussed in Section 3. In later sections we review various theoretical and computational methods which can be used to determine rovibrational resonance states of molecules. Section 4 introduces the reader to coupled-channels or close-coupling molecule-molecule scattering computations. Section 5 discusses the stabilization method, Section 6 reviews the complex absorbing potential techniques, while Section 7 is devoted to the complex coordinate scaling method. In all these sections we also briefly present examples of applications of the various methods, taken from previous studies of the authors. We summarize and conclude this Perspective and provide some future outlook of the expected development of the field in Section 8.

2 Elementary theory of resonance states

We are aware of a number of reviews, [77,96,97,100,136–139] proceedings, [140–142] and books [20,73,143–145] which deal with the definition, understanding, and determination of quasibound (resonance) states, as the topic of resonances has been popular since the 1970s. However, *rovibrational* resonance states have been discussed much less, especially visible is the lack of studies for systems with more than three atoms. For many larger systems reduced-dimensional treatments, offered by the use of certain Hamiltonians and computational techniques, [83,146,147] are viable. Nevertheless, even reduced-dimensional resonance studies of larger systems are rather scarce in the literature.

All numerical treatments of resonances agree that there are two principal types of rovibrational resonances: shape and Feshbach resonances. Note that shape resonances are also sometimes called "orbiting resonances". [32] Elementary models and examples for both of these resonance types will be discussed in this section in order to help the reader appreciate the formation and characterization of the rovibrational resonances discussed in later sections.

2.1 Shape resonances

Shape resonances arise as a consequence of the unique shape of potentials governing nuclear motion: in certain cases there exists a barrier along the dissociation coordinate whose height exceeds the dissociation energy. These barriers may arise either due to rotational excitation or to the crossing of two potential energy curves or surfaces. In what follows we mostly focus on the first possibility, on rotational barriers (see Fig. 1). If a quasibound state has an energy greater than the dissociation energy but less than the height of the potential energy barrier, the state is an example of a shape resonance; however, resonances above the barrier might also be formed, though usually with much shorter lifetimes. The states trapped behind the barrier will eventually dissociate via quantum tunneling. The lifetime of shape resonances depends on the height and shape of the potential energy barrier. The existence of shape resonances is a quantum phenomenon, because in the classical limit tunneling is forbidden and such resonances become bound states. Shape-type rovibrational resonances occur typically if the molecule is in a highly excited rotational state and a significant centrifugal barrier is formed.

The concept of shape resonances can be elucidated on a simple example, the case of a diatomic molecule. The Hamiltonian in the usual notation is

$$\hat{H} = -\frac{1}{2\mu R}\frac{d^2}{dR^2}R + V_{\text{eff}}(R), \qquad (3)$$

where

$$V_{\text{eff}}(R) = \frac{J(J+1)}{2\mu R^2} + V(R), \qquad (4)$$

μ is the reduced mass, and R is the internuclear distance. Fig. 1 shows the effective potential, $V_{\text{eff}}(R)$, of the OH radical, with a centrifugal barrier on the $J=40$ curve, where J is the rotational quantum number, and $V(R)$ is a Morse potential, with parameters taken from Ref. 148. The dissociation threshold of the OH radical is $D_0(\text{OH}^-)=39\,285$ cm^{-1}, while the top of the $J=40$ centrifugal barrier is at $41\,558$ cm^{-1}. In this simple example one can find
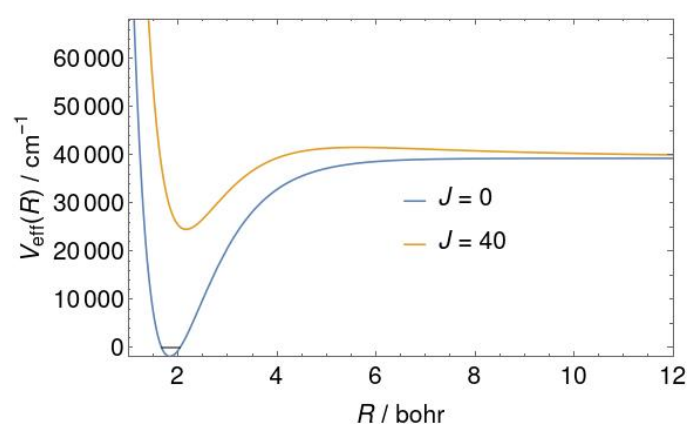

Fig. 1 Example for the formation of a centrifugal potential barrier in the case of a diatomic molecule, where J is the rotational quantum number. The effective potential, $V_{\text{eff}}(R)$, with parameters taken from Ref. 148, is that of the OH radical, where R is the OH distance, and the zero point vibrational energy is denoted with a horizontal line.

three shape resonances corresponding to $J = 40$: two of them, at $40\,250\ \text{cm}^{-1}$ and $41\,083\ \text{cm}^{-1}$ are long lived (where the imaginary part of the energy is almost zero), while the third one, at $41\,586\ \text{cm}^{-1}$, is a resonance above the barrier with an exceedingly short lifetime and a width (Γ) of $62\ \text{cm}^{-1}$.

2.2 Feshbach resonances

Feshbach-type rovibrational resonances occur when the molecular system has at least one extra degree of freedom (dof) besides the dissociation coordinate. This extra dof of the system allows to "store" the excess energy above the dissociation limit temporarily in a non-dissociative mode.

There is an intuitive way to view Feshbach-type resonances. This requires to start with a zeroth-order Hamiltonian in which the dissociative and non-dissociative dofs are uncoupled. For the uncoupled system, bound states (formed by excitations in the non-dissociative mode) are embedded in the sea of continuum-energy dissociative states formed along the dissociative mode. In an extended Hamiltonian couplings occur between the dissociative and non-dissociative degrees of freedom; thus, the eigenstates of the improved Hamiltonian are a mixture of the bound states and the continuum states of the zeroth-order Hamiltonian. The bound states are said to "dissolve" in the continuum. If the molecular system is in an excited bound state of the zeroth-order Hamiltonian at the beginning of the time evolution, it will not stay there forever, because the couplings allow transition to the continuum states. In the limit of infinite time evolution, the wave function of the system has zero bound-state component, *i.e.*, the system decays in time.

The simplest model of Feshbach resonances considers the coupling of one well-separated resonance state with a single continuum. Consideration of two or more non-separated, coupled resonances complicates the picture but does not result in qualitative differences. The case of several continua, corresponding to separate dissociation channels, coupled with a single resonance was considered both by Feshbach[6] and Fano.[26]

2.2.1 The Bixon–Jortner model

The Bixon–Jortner model[149] provides a simple analytic treatment of a Feshbach-type resonance. The "zeroth-order" Hamiltonian, $\hat{H}_0$, has a discrete eigenstate, $|\phi\rangle$, whose eigenenergy is E_ϕ,

$$\hat{H}_0 |\phi\rangle = E_\phi |\phi\rangle, \tag{5}$$

and continuum eigenstates $|k\rangle$ ($k \in \mathbb{Z}$) with energies $E_k = k\delta$,

$$\hat{H}_0 |k\rangle = E_k |k\rangle = k\delta |k\rangle. \tag{6}$$

The continuum eigenstates are discretized for the sake of this derivation, δ is the energy spacing between two neighboring discretized continuum states.

Let a small perturbation, $\hat{V}$, couple the discrete state to the continuum,

$$\langle \phi|\hat{V}|k\rangle = v \text{ and } \langle \phi|\hat{V}|\phi\rangle = \langle k|\hat{V}|k'\rangle = 0. \tag{7}$$

Fermi's golden rule[150] can be used to provide the transition rate

w_T from $|\phi\rangle$ to the continuum,

$$w_T = 2\pi|\langle k|\hat{V}|\phi\rangle|^2 \Pi(E_\phi) = 2\pi v^2 \frac{1}{\delta}, \tag{8}$$

where w_T is the transition probability per unit time and $\Pi(E_\phi)$ is the density of states at E_ϕ. To allow for the desired $\delta \to 0$ limit, w_T is kept constant within the Bixon–Jortner model; thus,

$$\frac{v^2}{\delta} = \frac{w_T}{2\pi} = \text{constant.} \tag{9}$$

We have to solve the TInSE for the full system,

$$\hat{H}|\psi_\mu\rangle = (\hat{H}_0 + \hat{V})|\psi_\mu\rangle = E_\mu |\psi_\mu\rangle. \tag{10}$$

The eigenstate, $|\psi_\mu\rangle$, is expanded on the basis of the eigenvectors of the "zeroth-order" Hamiltonian,

$$|\psi_\mu\rangle = \langle \phi|\psi_\mu\rangle |\phi\rangle + \sum_{l=-\infty}^{\infty} \langle l|\psi_\mu\rangle |l\rangle. \tag{11}$$

Substituting Eq. (11) into Eq. (10), then multiplying with $\langle k|$ or $\langle \phi|$ from the left and requiring that $\langle \psi_\mu|\psi_\mu\rangle = 1$, we obtain the following equations for the energy and the coefficients:

$$E_\mu = E_\phi + \sum_{k=-\infty}^{\infty} \frac{v^2}{E_\mu - \delta k}, \tag{12}$$

$$\langle \phi|\psi_\mu\rangle = \left[1 + \sum_{k=-\infty}^{\infty} \frac{v^2}{(E_\mu - \delta k)^2}\right]^{-1/2}, \tag{13}$$

and

$$\langle k|\psi_\mu\rangle = \frac{v\langle \phi|\psi_\mu\rangle}{E_\mu - \delta k}. \tag{14}$$

Taking advantage of the identities $\sum_{k=-\infty}^{\infty} 1/(z-k) = \pi \cot(\pi z)$ and $\sum_{k=-\infty}^{\infty} 1/(z-k)^2 = \pi^2/\sin^2(\pi z)$, we can rewrite the formulas as

$$\frac{2(E_\mu - E_\phi)}{w_T} = \cot\left(\frac{E_\mu \pi}{\delta}\right) \tag{15}$$

and

$$\langle \phi|\psi_\mu\rangle = \frac{v}{\sqrt{v^2 + (w_T/2)^2 + (E_\mu - E_\phi)^2}}. \tag{16}$$

Next, let us compare the eigenvalues E_μ to the eigenvalues of $\hat{H}_0$. The continuum of $\hat{H}_0$ is mostly perturbed close to E_ϕ. The states far from E_ϕ resemble the continuum states because $\langle \phi|\psi_\mu\rangle \approx 0$, and thus $E_\mu \approx E_k$ and $\langle k|\psi_\mu\rangle \approx 1$. The transition rate, w_T, determines how many states are perturbed: if w_T is large, the perturbation will be significant in a wide energy range.

Now, let us calculate what is the probability of finding the system in $|\phi\rangle$ if E_μ is in the $(E, E + dE]$ energy range:

$$dN_\phi = \sum_{E < E_\mu \le E + dE} |\langle \phi|\psi_\mu\rangle|^2 \approx \frac{dE}{\delta} \frac{v^2}{v^2 + (w_T/2)^2 + (E - E_\phi)^2}. \tag{17}$$

Then, by taking the $\delta \to 0$ and $v^2 \to 0$ limits, such that v^2/δ is constant (Eq. (9)), we obtain

$$\frac{dN_\phi}{dE} = \frac{1}{\pi} \frac{w_T/2}{(w_T/2)^2 + (E - E_\phi)^2}, \tag{18}$$
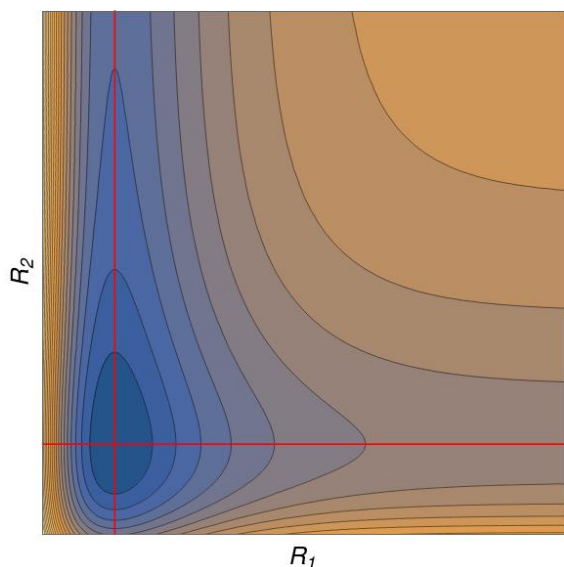
Fig. 2 Contour plot of the $V(R_1, R_2)$ potential of a A–A–B linear molecule, chosen as an example of Feshbach resonances, see Sec. 2.2.2. R_1 and R_2 are the A–A and A–B bond lengths, respectively, and the A–B bond is weaker than the A–A bond. The red lines denote the equilibrium values of R_1 and R_2.

which is a Lorentzian distribution. Thus, the discrete state is indeed "dissolved" in the continuum.

Let us now turn our attention to the time evolution of the system, starting from the state $|\phi\rangle$ at $t = 0$. If

$$|\Psi(t=0)\rangle = |\phi\rangle = \sum_\mu \frac{v}{\sqrt{v^2 + (w_T/2)^2 + (E_\mu - E_\phi)^2}} |\psi_\mu\rangle, \quad (19)$$

then

$$|\Psi(t)\rangle = \sum_\mu \frac{v}{\sqrt{v^2 + (w_T/2)^2 + (E_\mu - E_\phi)^2}} e^{-iE_\mu t} |\psi_\mu\rangle. \quad (20)$$

The overlap of $|\Psi(t)\rangle$ and $|\phi\rangle$ is

$$\langle\phi|\Psi(t)\rangle = \sum_\mu \frac{v^2}{v^2 + (w_T/2)^2 + (E_\mu - E_\phi)^2} e^{-iE_\mu t} \quad (21)$$

$$= \sum_\mu \frac{w_T}{2\pi} \frac{1}{v^2 + (w_T/2)^2 + (E_\mu - E_\phi)^2} \delta e^{-iE_\mu t}. \quad (22)$$

The sum can be approximated with an integral by taking the $\delta \to 0$ and $v^2 \to 0$ limits. Then,

$$\langle\phi|\Psi(t)\rangle \approx \int_{-\infty}^{\infty} \frac{w_T}{2\pi} \frac{e^{-iEt}}{(w_T/2)^2 + (E - E_\phi)^2} dE = \begin{cases} e^{-iE_\phi t - w_T t/2} \text{ if } t \geq 0 \\ e^{-iE_\phi t - w_T |t|/2} \text{ if } t < 0. \end{cases} \quad (23)$$

The probability of finding the system in state $|\phi\rangle$ decreases exponentially:

$$|\langle\phi|\Psi(t)\rangle|^2 = e^{-w_T t}; \quad (24)$$

thus, the system decays exponentially.

2.2.2 The model of two coupled oscillators

Vibrational Feshbach resonances occur if two bonds of a molecule have very different strengths. Let us consider a linear A–A–B molecule, with atomic masses m_A and m_B, where the A–A and A–B distances are denoted by R_1 and R_2, respectively, and the A–B bond is significantly weaker than the A–A bond. Neglecting the bending dof, the vibrational Hamiltonian of the system, employing reduced masses μ $(\mu_{ij} = m_i m_j / (m_i + m_j))$, becomes

$$\hat{H} = -\frac{1}{2\mu_{AA}} \frac{\partial^2}{\partial R_1^2} - \frac{1}{2\mu_{AB}} \frac{\partial^2}{\partial R_2^2} + \frac{1}{m_A} \frac{\partial^2}{\partial R_1 \partial R_2} + V(R_1, R_2), \quad (25)$$

where a contour plot of the potential $V(R_1, R_2)$ is seen in Fig. 2. We define the operators $\hat{H}^{AA}$ and $\hat{H}^{AB}$ as

$$\hat{H}^{AA} = -\frac{1}{2\mu_{AA}} \frac{\partial^2}{\partial R_1^2} + V_{AA}(R_1) \quad (26)$$

and

$$\hat{H}^{AB} = -\frac{1}{2\mu_{AB}} \frac{\partial^2}{\partial R_2^2} + V_{AB}(R_2), \quad (27)$$

where $V_{AA}(R_1)$ and $V_{AB}(R_2)$ are one-dimensional cuts of the potential (see Fig. 3), while assuming that the other coordinate takes its equilibrium value. The "zeroth-order" Hamiltonian of the system is then

$$\hat{H}_0 = \hat{H}^{AA} + \hat{H}^{AB}. \quad (28)$$

The perturbation term that couples the A–A and A–B oscillators is

$$\hat{V}_{int} = \hat{H} - \hat{H}_0 = \frac{1}{m_A} \frac{\partial^2}{\partial R_1 \partial R_2} + V(R_1, R_2) - V_{AA}(R_1) - V_{AB}(R_2), \quad (29)$$

which contains the mixed derivatives and the $R_1 - R_2$ correlation of the potential.

Let two bound eigenstates of $\hat{H}^{AA}$ be $|\phi_0\rangle$ and $|\phi_1\rangle$ with E_0^{AA} and E_1^{AA} eigenenergies, respectively, where E_0^{AA} is below the dis-
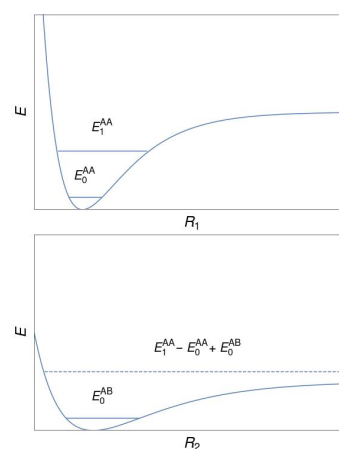

Fig. 3 $V_{AA}(R_1)$ (left panel) and $V_{AB}(R_2)$ (right panel), one-dimensional cuts of $V(R_1, R_2)$ (see Fig. 2) at the equilibrium value of R_2 and R_1, respectively. When the one-dimensional oscillators corresponding to $V_{AA}(R_1)$ and $V_{AB}(R_2)$ are coupled, a resonance is formed with $E_1^{AA} + E_0^{AB}$.

sociation threshold along R_2 but E_1^{AA} is above that:

$$\hat{H}^{AA}|\phi_n(R_1)\rangle = E_n^{AA}|\phi_n(R_1)\rangle. \tag{30}$$

A bound eigenstate of $\hat{H}^{AB}$ is $|\chi_0\rangle$, with E_0^{AB} energy, and there are $|\chi_{E^{AB}}^{cont}\rangle$ continuum eigenvectors:

$$\hat{H}^{AB}|\chi_0(R_2)\rangle = E_0^{AB}|\chi_0(R_2)\rangle \tag{31}$$

and

$$\hat{H}^{AB}|\chi_{E^{AB}}^{cont}(R_2)\rangle = E^{AB}|\chi_{E^{AB}}^{cont}\rangle(R_2). \tag{32}$$

The eigenvectors of $\hat{H}_0$ of Eq. (28) are the direct product of the AA and AB eigenvectors of Eqs. (30)–(32). We can construct a discrete and a continuum state of $\hat{H}_0$ that have the same energy:

$$\hat{H}_0\left(|\phi_1\rangle \otimes |\chi_0\rangle\right) = (E_1^{AA}+E_0^{AB})\left(|\phi_1\rangle \otimes |\chi_0\rangle\right) \tag{33}$$

and assuming that $E_1^{AA}-E_0^{AA}+E_0^{AB}$ is in the continuum spectrum of $\hat{H}^{AB}$ (see Fig. 3),

$$\hat{H}_0\left(|\phi_0\rangle \otimes |\chi_{(E_1^{AA}-E_0^{AA}+E_0^{AB})}^{cont}\rangle\right) = (E_1^{AA}+E_0^{AB})\left(|\phi_0\rangle \otimes |\chi_{E_1^{AA}-E_0^{AA}+E_0^{AB}}^{cont}\rangle\right). \tag{34}$$

The continuum and the discrete states are coupled by the $\hat{V}_{int}$ term,

$$\langle\phi_1\chi_0|\hat{V}_{int}|\phi_0\chi_{E_1^{AA}-E_0^{AA}+E_0^{AB}}^{cont}\rangle = \left(\langle\phi_1|\otimes\langle\chi_0|\right)\hat{V}_{int}\left(|\phi_0\rangle\otimes|\chi_{E_1^{AA}-E_0^{AA}+E_0^{AB}}^{cont}\rangle\right) \tag{35}$$

Based on the Bixon–Jortner model, if the system is initially in the discrete state $|\Psi(t=0)\rangle = |\phi_1\rangle \otimes |\chi_0\rangle$, it is the coupling $\hat{V}_{int}$ which allows the transition to the continuum. This means that the weaker A–B bond breaks up and the molecule dissociates. The probability of finding the molecule in the discrete state $|\Psi(t=0)\rangle$ decays exponentially,

$$|\langle\Psi(t=0)|\Psi(t)\rangle|^2 = e^{-w_T t}, \tag{36}$$

where

$$w_T = 2\pi|\langle\phi_1\chi_0|\hat{V}_{int}|\phi_0\chi_{E_1^{AA}-E_0^{AA}+E_0^{AB}}^{cont}\rangle|^2\Pi(E_1^{AA}+E_0^{AB}), \tag{37}$$

and $\Pi(E_1^{AA}+E_0^{AB})$ denotes the density of states for the continuum of $\hat{H}_0$ at energy $E_1^{AA}+E_0^{AB}$. Based on this simple example, vibrational Feshbach resonances are formed if (a) one bond of the molecule is significantly weaker than the others, so the vibration along this bond is a dissociative dof, and (b) the potential or the cross-derivative terms of the kinetic-energy operator couple the dissociative dof and the vibrational modes of the strong bonds. The resonance lifetime is thus determined by the coupling term of the potential and the appropriate mixed derivatives in the kinetic energy operator.

2.2.3 Weakly-bound dimers

Feshbach resonances occur very commonly, and they have been measured spectroscopically for a large number of weakly-bound dimers.[23,151–154] Let us consider a van der Waals (vdW) dimer formed by a strongly bound diatomic molecule, AB, and an atom, X. The structure and dynamics of the vdW dimer is described conveniently by Jacobi coordinates, where r is the A–B distance, R is the distance between atom X and the center of mass (COM) of

the AB unit, and θ is the angle between the $\mathbf{r}$ and $\mathbf{R}$ vectors. If we keep r fixed, the Hamiltonian is simply

$$\hat{H} = \frac{1}{2\mu}\left(-\frac{1}{R}\frac{\partial^2}{\partial R^2}R + \frac{\hat{l}^2(\hat{\mathbf{R}})}{R^2}\right) + B_{rot}\hat{j}^2(\hat{\mathbf{r}}) + V(R,\theta), \tag{38}$$

where B_{rot} is the rotational constant of the AB molecule, and $\hat{j}(\hat{\mathbf{r}})$ and $\hat{l}(\hat{\mathbf{R}})$ are the angular momentum operators for the rotation of the AB molecule and the diatom formed by the X atom and the COM of the AB unit, respectively. The unit vectors $\hat{\mathbf{R}}$ and $\hat{\mathbf{r}}$ define the polar angles of the vectors $\mathbf{R}$ and $\mathbf{r}$, respectively. The "zeroth-order" Hamiltonian is $\hat{H}_0 = \hat{H}^{AB-X} + \hat{H}^{AB}$, where

$$\hat{H}^{AB-X} = \frac{1}{2\mu}\left(-\frac{1}{R}\frac{\partial^2}{\partial R^2}R + \frac{\hat{l}^2(\hat{\mathbf{R}})}{R^2}\right) + V_{AB-X}(R), \tag{39}$$

and $V_{AB-X}(R)$ is a one-dimensional cut of the potential at (usually) the equilibrium value of θ, and

$$\hat{H}^{AB} = B_{rot}\hat{j}^2(\hat{\mathbf{r}}). \tag{40}$$

The perturbation that couples the two subsystems is

$$\hat{V}_{int} = V(R,\theta) - V_{AB-X}(R), \tag{41}$$

which contains the θ-dependent part of the potential. The eigenstates of the rotating AB unit are the spherical harmonic functions,

$$\hat{H}^{AB}|Y_j^m\rangle = E_j^{AB}|Y_j^m\rangle = B_{rot}j(j+1)|Y_j^m\rangle. \tag{42}$$

$\hat{H}^{AB-X}$ has both bound and continuum eigenstates,

$$\hat{H}^{AB-X}|\chi_n(R)\rangle = E_n^{AB-X}|\chi_n(R)\rangle \tag{43}$$

and

$$\hat{H}^{AB-X}|\chi_{E^{AB-X}}^{cont}(R)\rangle = E^{AB-X}|\chi_{E^{AB-X}}^{cont}(R)\rangle. \tag{44}$$

If the AB–X interaction is weak, there can be low-lying rotationally excited states of $\hat{H}^{AB}$ that have an energy greater than the dissociation threshold of the dimer, D_0. Let us assume that $D_0 < E_0^{AB-X} + E_{j_2}^{AB} - E_{j_1}^{AB}$ and $E_{j_1}^{AB} < D_0 < E_{j_2}^{AB}$, where E_0^{AB-X} corresponds to the ground state of $\hat{H}^{AB-X}$. We can then construct a discrete and a continuum eigenstate of $\hat{H}_0 = \hat{H}^{AB} + \hat{H}^{AB-X}$, defined similar to Eq. (28), that have the equal energy, $E_{j_2}^{AB} + E_0^{AB-X}$:

$$\hat{H}_0\left(|Y_{j_2}^{m_2}\rangle \otimes |\chi_0\rangle\right) = (E_{j_2}^{AB}+E_0^{AB-X})\left(|Y_{j_2}^{m_2}\rangle \otimes |\chi_0\rangle\right) \tag{45}$$

and

$$\hat{H}_0\left(|Y_{j_1}^{m_1}\rangle \otimes |\chi_{(E_0^{AB-X}+E_{j_2}^{AB}-E_{j_1}^{AB})}^{cont}\rangle\right) = \tag{46}$$

$$(E_{j_2}^{AB}+E_0^{AB-X})\left(|Y_{j_1}^{m_1}\rangle \otimes |\chi_{(E_0^{AB-X}+E_{j_2}^{AB}-E_{j_1}^{AB})}^{cont}\rangle\right).$$

We can now derive the time evolution of the system starting from the discrete state. If $|\Psi(t=0)\rangle = |Y_{j_2}^{m_2}\rangle \otimes |\chi_0\rangle$, then

$$|\langle\Psi(t=0)|\Psi(t)\rangle|^2 = e^{-w_T t} \tag{47}$$

where

$$w_{\mathrm{T}} = 2\pi | \langle Y_{j_2}^{m_2} \chi_0 | \hat{V}_{\mathrm{int}} | Y_{j_1}^{m_1} \chi_{(E_0^{\mathrm{AB-X}} + E_{j_2}^{\mathrm{AB}} - E_{j_1}^{\mathrm{AB}})}^{\mathrm{cont}} \rangle |^2 \Pi(E_{j_2}^{\mathrm{AB}} + E_0^{\mathrm{AB-X}}). \tag{48}$$

This simple example can be extended straightforwardly to explain the origin of Feshbach resonances in weakly-bound dimers, if some rovibrational eigenenergies of one monomer are greater than the dissociation energy of the dimer. The lifetime of a resonance is determined by the coupling of the monomer motions and the intermonomer stretching. We present examples for vdW complexes supporting Feshbach resonances in the Application subsections of several later sections. Interested readers can find a vast amount of additional examples on the Feshbach resonances of vdW complexes in the literature, for representative early works the related chapter in Ref. 142 might be consulted.

2.3 The non-Hermitian picture

As discussed in the previous subsections, in Hermitian QM resonance states can be associated with wave packets involving continuum states.[73] Non-Hermitian QM offers a different perspective on quasibound states.

In the NHQM case, quasibound states are expressed as stationary solutions of the time-dependent Schrödinger-equation, *i.e.*, the total wave function is written as the product of a coordinate-dependent and a time-dependent part. That is, in atomic units,

$$\Psi_n^{\mathrm{res}}(\mathbf{q},t) = \Psi_n^{\mathrm{res}}(\mathbf{q}) \exp(-iE_n^{\mathrm{res}} t) \tag{49}$$

and

$$\hat{H} \Psi_n^{\mathrm{res}}(\mathbf{q}) = E_n^{\mathrm{res}} \Psi_n^{\mathrm{res}}(\mathbf{q}) \tag{50}$$

hold. The time dependence of resonance states is described by assuming that the probability of finding the system at a certain $\mathbf{q}$ coordinate point has an exponential decay in time, see Eq. (2). Eqs. (2) and (49) are simultaneously satisfied if the energy is complex, $E_n^{\mathrm{res}} = \varepsilon_n - \frac{i}{2}\Gamma_n$, implying that the wave function diverges exponentially along the dissociation coordinate (thus, it is not in the L^2 space).

According to the uncertainty principle relating time and energy, the finite lifetime of resonance states results in an uncertainty in the resonance energy, and the density of states near the resonance energy has a Lorentzian distribution,[155,156]

$$\Pi^{\mathrm{res}}(E) = \frac{1}{\pi} \frac{\Gamma_n/2}{(E-\varepsilon_n)^2 - \Gamma_n^2/4}. \tag{51}$$

Note that the quantity w_{T} of the previous subsections plays a very similar role to Γ_n, which can be seen by comparing Eq. (2) to Eq. (24), as well as Eq. (51) to Eq. (18).

2.4 Resonances in molecule-molecule scattering

Direct access to rotational-vibrational resonances is provided in molecule-molecule (or molecule-atom) collisions. When the colliding molecules approach each other and get to the region where their interaction becomes attractive, the lowering of the potential energy and the conservation of total energy imply that their relative kinetic energy increases. Specific collision energies fa-

cilitate the formation of quasi-bound states of the collision complex, in which the excess kinetic energy is temporarily stored in the end-over-end rotation of the complex (a shape resonance) or in a higher rotational or vibrational state of one or both of the colliding molecules (a Feshbach resonance). Eventually the quasi-bound states dissociate and the molecules fly apart, either in their original rovibrational state but possibly with exchange of momentum (elastic collisions) or in different rovibrational states (inelastic collisions). The state-to-state integral scattering cross sections measure the probability that the collision has led to one of these events. The corresponding differential cross sections measure these probabilities as a function of the scattering angle, *i.e.*, the angle between the trajectories of the molecules flying apart. When a quasi-bound state or scattering resonance appears, the collision complex lives (much) longer than the normal collision time and the probability that "something happens" during the collision increases. Since this occurs only at specific collision energies, this causes peaks in the ICSs as function of the collision energy, which can be directly observed. The formation of a long-lived collision complex will also strongly affect the scattering angle, but it is not obvious how. Measuring and computing DCSs at resonances provide interesting insight into the collision process.

The various methods to analyze the resonances found in coupled-channel computations are explained in detail in Sec. 4. In anticipation, an illustrative discussion, based on the theory developed in the 1930s by Breit and Wigner[4] and Siegert,[5] is given next.

The calculated and observed ICSs and DCSs are assumed to result from an interference between resonance and background contributions. These contributions can be disentangled by applying a theoretical analysis similar to Feshbach–Fano partitioning.[157,158] The energy-dependent multichannel **S**-matrix is written as[20]

$$\mathbf{S}(E) = \mathbf{S}^{\mathrm{bg}}(E) \mathbf{U}^{\mathrm{res}}(E), \tag{52}$$

where the background contribution $\mathbf{S}^{\mathrm{bg}}(E)$ is a slowly varying function of the collision energy E and the resonance contribution is given by the Breit–Wigner formula

$$\mathbf{U}^{\mathrm{res}}(E) = \mathbf{I} - \frac{2i\mathbf{A}}{E - E_{\mathrm{res}} + i\Gamma/2}, \tag{53}$$

where E_{res} is the energy of the resonance, Γ is its width (the inverse lifetime), and the complex-valued matrix elements $A_{\alpha\beta} = a_\alpha a_\beta^*$ contain the partial widths a_α obeying the relation $\sum_\alpha |a_\alpha|^2 = \Gamma/2$. The idea associated with the Breit–Wigner formula is that in the complex energy plane, where the bound states correspond to poles of the S-matrix on the negative real energy axis, resonances are represented by poles below the positive real axis at positions $E_{\mathrm{res}} - i\Gamma/2$ (see Eq. (1)).

By analyzing the energy dependence of the matrix elements of **S** in the range of each resonance with an algorithm described in the Supplement of Ref. 47, one can determine the parameters E_{res}, Γ, and a_α. Then, one can separate the resonance contributions to the scattering matrix $\mathbf{S}(E)$ from the background and apply the usual expressions[159] to compute ICSs and DCSs from
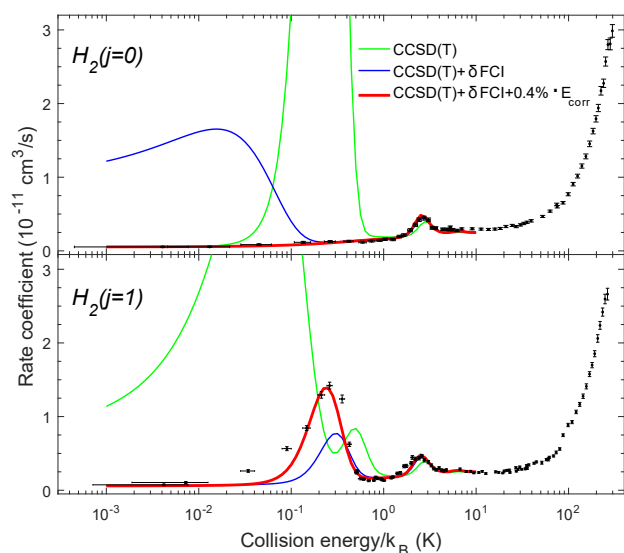
Fig. 4 Experimental and theoretical Penning ionization rate coefficients of *para*- and *ortho*-H_2 molecules in collisions with He$^*(2^3S_1)$.[51] The experimental rate coefficients are presented as black dots with error bars. The upper and lower panels correspond to *para*-H_2 ($j = 0$) and *ortho*-H_2 ($j = 1$), respectively. Two shape resonances are observed below 5 K for the reaction with *ortho*-H_2 at 2.37 ± 0.09 K and at 270 ± 20 mK, while the reaction with *para*-H_2 yields only the higher-energy resonance. The results of state-of-the-art first-principles computations are depicted by the green, blue, and red curves in both panels. The interaction potential obtained with the current "gold standard" of electronic-structure methods, coupled cluster theory at the [CCSD(T) /aug-cc-pV6Z+mid-bond, green] level, alone erroneously predicts a low-energy resonance for *para*-H_2 and two low-energy resonances for *ortho*-H_2. Including a full configuration interaction (FCI /aug-cc-pVQZ) correction (blue) improves the agreement down to collision energies corresponding to a few hundred milli-Kelvin. Further improvement of the interaction potential is achieved by uniformly scaling the correlation energy by 0.4 % (red), resulting in excellent agreement with the measured resonance positions and the overall behavior of the rate coefficient down to the lowest collision energies. The calculated rate coefficients are convoluted with the experimental resolution (8 mK) for the lowest collision energies. This figure is reproduced from Ref. 51.

the **S**-matrix, with or without resonance contributions. This is very instructive, especially since it shows explicitly the effects of a resonance on the DCS, which is not obvious intuitively.

3 On potentials supporting resonance state computations

Both spectroscopic and quantum-scattering computations of rotational-vibrational resonance states indicated repeatedly that the energies, and even more so the lifetimes, are extremely sensitive to fine details of the asymptotic parts of the PESs utilized for these computations.[51,66,160] There are not that many potentials available for strongly-bound molecules which can be used to compute rovibrational resonance states of polyatomic molecular systems accurately. The basic problem here and in scattering reactions is the proper description of the long-range interaction part of the potential for chemically interesting systems. These problems become especially pronounced for cold and ultracold chemistry.

Molecule-molecule scattering resonances, especially just above the dissociation threshold, are not only sensitive to the shape of the vdW well in the interaction potential, but also to its depth. This implies that the possibility of measuring molecule-molecule scattering resonances for very low collision energies and with high energy resolution is extremely useful to critically check that the shape and well depth of anisotropic intermolecular potentials are indeed accurate. This was recently demonstrated especially vividly for NO–He and NO–H_2 scattering.[66] It was shown that potentials calculated with the *ab initio* coupled-cluster method including single and double excitations with a perturbative estimate of triples [CCSD(T)],[161] which is considered to be the "gold standard" of electronic-structure theory, were not sufficiently accurate to obtain agreement between the observed resonances and those from well-converged coupled-channels computations that used these potentials. For resonances at even lower collision energy it was explicitly confirmed[116] that the intermolecular potential had to be calculated at a higher level of electron correlation, with the full inclusion of triple excitations and a perturbative estimate of quadruples [CCSDT(Q)],[162] to compute ICSs and DCSs that reproduce the experimental data at these resonances.

Another example of low-energy scattering resonances being extremely sensitive to the accuracy of the potential used in coupled-channels computations was provided by merged-beam experiments for collisions of H_2 molecules with $^3S_1$ excited He atoms, leading to Penning ionization.[51] An interesting observation was that for collisions with *para*-H_2 ($j = 0$) and *ortho*-H_2 ($j = 1$) the same resonance was observed at 2.37 K, but another resonance, at 270 mK, occurred only in collisions with *ortho*-H_2. Both resonances were also found in coupled-channels computations, but the one at 270 mK could only be reproduced when using an *ab initio* potential surface for H_2–He* with corrections calculated at the full configuration-interaction (FCI) level and a further scaling of the correlation energy by 0.4 %, see Fig. 4.

4 Resonances in molecule-molecule scattering

Let us begin by discussing the computation and characterization of resonances with the top-down (scattering) approach; in the subsequent sections 5 to 7 of this Perspective we discuss the several bottom-up (spectroscopic) approaches to the computation of resonance states. In the top-down approach the energy is usually set to zero at the dissociation limit, while in bottom-up computations the energy zero is conveniently chosen as the energy of the ground vibrational state (deviating from the bottom of the PES by the zero-point vibrational energy).

4.1 The coupled-channels (CC) method

The Hermitian Hamiltonian used in CC calculations, which is a generalization of the atom-diatom Hamiltonian of Sec. 2.2.3, is given both in space-fixed (SF) and body-fixed (BF) coordinates in Ref. 163 for two rigid arbitrary polyatomic molecules. Next, a coupled channel basis $\varphi_{\mathbf{n},l}^{(J)}(\rho)$, which depends on all coordinates ρ of the system except the scattering coordinate R, needs to be defined. The index $\mathbf{n}$ labels the products of the coupled rota-

tional states of the colliding molecules A and B, l is related to the end-over-end angular momentum of the A–B complex, and J is a quantum number corresponding to the total angular momentum obtained by coupling l with the rotational angular momenta of A and B. The $\varphi_{\mathbf{n},l}^{(J)}(\rho)$ basis, expressed in SF coordinates, is written for the general case of collisions between two arbitrary polyatomic molecules in Ref. 163, where the corresponding basis in BF coordinates is also given. The matrix elements of the Hamiltonian over both the SF and the BF bases are specified there, as well. The scattering wave function is expanded in the channel basis as

$$\psi^{(J)}(R,\rho) = \sum_{\mathbf{n},l} \phi_{\mathbf{n},l}^{(J)}(R)\,\varphi_{\mathbf{n},l}^{(J)}(\rho); \qquad (54)$$

the R-dependent "expansion coefficients" are the radial wave functions of each channel. Substitution of this wave function into the time-independent Schrödinger equation, multiplication with the complex conjugate channel basis functions $\varphi_{\mathbf{n}',l'}^{(J)*}(\rho)$, and integration over all coordinates ρ yields a set of coupled second-order differential equations for the radial wave functions, the CC equations,[20,159] which are solved numerically. The total angular momentum is a conserved quantity, so the computations can be performed separately for each J.

The incoming wave in a certain direction is a plane wave and the radial wave functions must obey so-called S-matrix boundary conditions at large R. When the incoming plane wave is expanded in spherical waves with angular momentum l, the partial wave index, and the outgoing wave is written as a linear combination of spherical waves with angular momenta l', it follows that the radial wave functions must have the following asymptotic form,

$$-\exp\left[-i(k_{\mathbf{n}}R - l\pi/2)\right]\delta_{\mathbf{n}',\mathbf{n}}\delta_{l',l} + \exp\left[i(k_{\mathbf{n}'}R - l'\pi/2)\right]S_{\mathbf{n}',l',\mathbf{n},l}^{(J)}. \quad (55)$$

The first term of Eq. (55) is an incoming spherical wave with wave number $k_{\mathbf{n}} = \sqrt{2\mu(E - \varepsilon_{\mathbf{n}})}$, where $E - \varepsilon_{\mathbf{n}}$ is the kinetic energy in channel $\mathbf{n}$, and μ is the reduced mass. The second term includes the corresponding outgoing waves with amplitudes $S_{\mathbf{n}',l',\mathbf{n},l}^{(J)}$, which are the elements of the scattering matrix $\mathbf{S}^{(J)}$. The latter are obtained by matching the solutions of the CC equations at large R with the expression in Eq. (55).

The state-to-state cross sections, which quantify the probabilities that the collision (de-)excites the molecules to specific final states when they start in a given initial state, are obtained from the elements of the transition matrix $\mathbf{T} = \mathbf{I} - \mathbf{S}$, with $\mathbf{I}$ being the unit matrix. The state-to-state ICSs are simply

$$\sigma_{\mathbf{n}\to\mathbf{n}'} = \frac{\pi}{k_{\mathbf{n}}^2(2j_A+1)(2j_B+1)}\sum_J (2J+1)\sum_{l,l'} |T_{\mathbf{n}',l',\mathbf{n},l}^{(J)}|^2, \quad (56)$$

where j_A and j_B are the angular momenta of molecules A and B in their initial state $\mathbf{n}$. Calculation of the DCSs is more complicated;[159] it involves a linear combination of scattering amplitudes that contain the T-matrix elements multiplied by spherical harmonics depending on the scattering angle, for all values of l, l', and J. The DCSs are proportional to the absolute square of this linear combination, so they also contain interferences from different l, l', and J values.

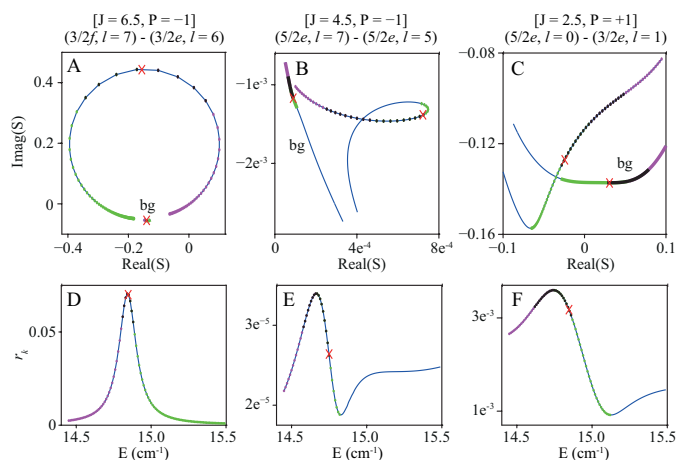Computer codes available for CC scattering computations in-

Fig. 5 Plots of some S-matrix elements in the complex plane and of the corresponding values of $r_k = |S_{k+1} - S_k|$ on the energy grid. Panels A, B, and C show examples of the different behavior of the matrix elements for various values of the total angular momentum J and parity P. The initial and final $j, e/f$ states of NO and the incoming and outgoing partial wave quantum numbers l are shown at each panel. Panels D, E, and F show the energy dependence of the r_k corresponding to panels A, B, and C, respectively, with the same colors of the dots. The curves labeled "bg" is the background matrix $\mathbf{S}^{\mathrm{bg}}$. The red cross marks the resonance energy E_{res}, the black dots indicate the region around the resonance where the second derivative of r_k is negative. The magenta/green colors indicate the regions around the resonance where the slope of r_k is positive/negative. This figure is reproduced from the Supplement of Ref. 47.

clude MOLSCAT,[164] Hibridon,[165] and TwoBC.[166] They solve the CC equations with a combination of the log-derivative propagator[167] at shorter distances and the Airy propagator[168,169] for larger R. Another CC program package was developed in the Nijmegen Theoretical Chemistry group, it uses the renormalized Numerov propagator.[170,171] It can also compute the bound rovibrational states of complexes including two weakly interacting molecules from the same Hamiltonian and the same channel basis, extended with a set of basis functions in R.[163]

The Hamiltonian and the channel basis described above are valid for rigid molecules. When vibrationally inelastic processes are considered, the Hamiltonian of Ref. 163 must be extended with the monomer vibrational Hamiltonians containing the appropriate kinetic energy operators and intramolecular potential hypersurfaces, and the intermolecular potential surface depending on the distance R and the orientations of the monomers must be made dependent also on their internal coordinates. Furthermore, the channel basis must be extended, by including the vibrational wave functions of the colliding molecules depending on their internal coordinates.

4.2 Analysis and characterization of resonances
4.2.1 Disentangling resonant and background scattering

As mentioned at the end of Sec. 2.4, the resonant contribution to ICSs and DCSs can be separated from the background by analyzing the energy dependence of the $\mathbf{S}$-matrix elements. This is illustrated in Ref. 47 for scattering resonances observed and cal-
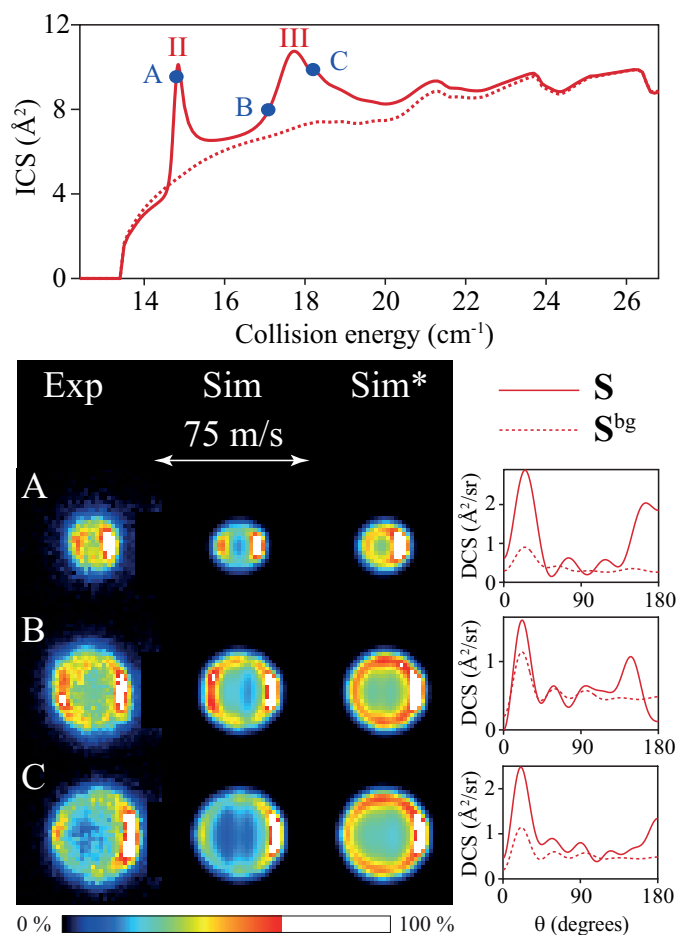
Fig. 6 Effect of the resonances on the cross sections for inelastic $(1/2f) \rightarrow (5/2f)$ NO–He scattering. The ICS is shown in the upper part, the DCSs below. Solid lines represent the complete theoretical ICS and DCSs, dashed lines the cross sections obtained when only the background scattering matrix $\mathbf{S}^{bg}$ in Eq. (52) is included for resonances. The lower panels show the measured (Exp) and simulated images based on either the complete DCSs (Sim) or the DCSs computed with the scattering matrix $\mathbf{S}^{bg}$ only (Sim*) for the experimental collision energies of (A) 14.8 cm^{-1}, (B) 17.1 cm^{-1}, and (C) 18.2 cm^{-1}. This figure is reproduced from Ref. 47.

Fig. 7 Phase-shift sums Φ (top panel) and corresponding lifetimes (lower panel) as a function of the collision energy, calculated for NH$_3$–He scattering.[174] The different curves correspond to different total angular momenta J, with the two curves for each J corresponding to even and odd overall parity. This figure is reproduced from Ref. 174.

culated for NO–He at collision energies between 13 and 20 cm^{-1}. Section 5 of the Supplement of Ref. 47 explains in detail how the elements of the **S**-matrix are analyzed and how the resonant contribution is separated from the background. As Fig. 5 illustrates, this is done for individual elements of the **S**-matrix that correspond to specific initial and final rotational states of NO. It is interesting to observe in Fig. 5 that the energy dependence of the real and imaginary part of the **S**-matrix elements resembles the behavior of the complex energy eigenvalues of Fig. 11, *vide infra*, obtained with complex absorbing potentials. When the individual **S**-matrix elements are thus disentangled, the effect of a resonance on the ICSs and DCSs of all state-to-state inelastic processes can be calculated explicitly. The upper panel of Fig. 6 shows that, indeed, the resonant peaks in the ICS disappear when the resonance contribution is removed, while the DCSs in the lower picture show that the resonances cause additional strong
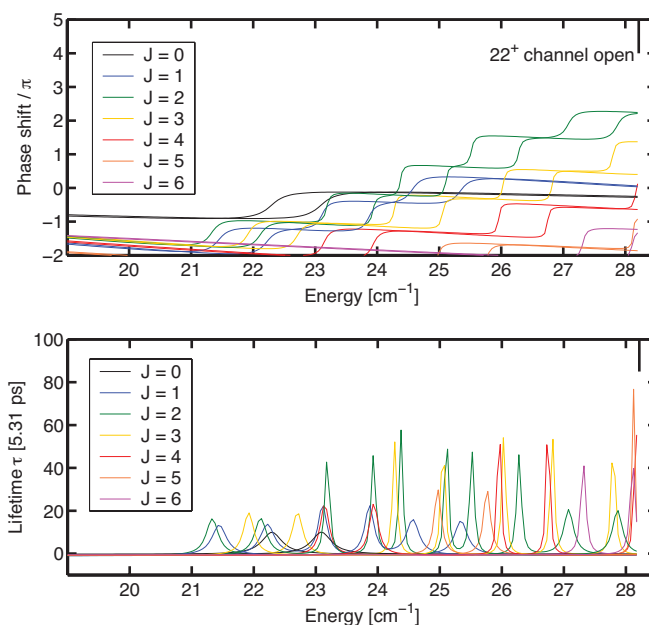
backward and near-forward scattering. Also the measured VMI images are shown, next to simulated images obtained from the calculated DCSs, with and without the resonant contributions. It is clear that the agreement with the measurements is much less satisfactory for the latter, which confirms that the experiment indeed detects resonance effects.

4.2.2 Phase shifts and resonance lifetimes

In a single-channel problem the **S**-matrix can simply be written as $\exp(2i\phi)$, with the angle ϕ being the phase shift. In the multi-channel case **S** is a unitary matrix, its eigenvalues can be written as $\exp(2i\phi_{\mathbf{n},l}^{(J)})$, and the phase-shift sum Φ is the sum of $\phi_{\mathbf{n},l}^{(J)}$ over all open channels.

It follows from theory[4,5] that when a resonance occurs the phase shift (sum) rapidly increases by π as a function of the collision energy E.[172,173] This is illustrated in the top panel of Fig. 7 for the example of NH$_3$–He scattering.[174] Similar results were obtained for NH$_3$–H$_2$ scattering[175] and OH–He scattering.[63] The derivative of the phase shift with respect to the energy, $\tau = \hbar d\Phi/dE$, gives the lifetime of the collision complex.[172,173] These lifetimes are shown in the lower panel of Fig. 7. This figure illustrates that at the energies where resonances occur one gets a long-lived collision complex. By comparing the peaks in this figure with the corresponding resonance peaks in the ICS (not shown for this example), one observes that the narrower the resonance peak in the ICS, *i.e.*, the smaller its width Γ, the longer its lifetime. This clearly confirms the relation $\tau = 1/\Gamma$.

4.2.3 Adiabatic-bender model

The adiabatic-bender model, proposed by Alexander *et al.*[176,177] and based on the Born–Oppenheimer angular-radial separation (BOARS),[178] characterizes scattering resonances by adiabatically separating the radial motion from the other dofs. The Hamiltonian matrix without the radial kinetic energy term is diagonalized for all values of R, which yields a set of one-dimensional (1D) potentials depending on R, the adiabatic-bender curves. These curves asymptotically connect to the states of the separated monomers. In the next step one obtains 1D scattering states by solving 1D scattering equations with each of these adiabatic potentials. If the adiabatic bender curves are sufficiently well separated and do not change their character by avoided crossings, the full-dimensional scattering states can be associated with the 1D states on each of the adiabatic bender curves and their character follows for the monomer states to which the curves connect asymptotically. Thus, in the case of resonances, it can be determined which monomer states participate in the resonance.

A recent example illustrating this method for OH–He and OH–Ne rotationally inelastic collisions is described in Ref. 63. The OH monomer has a large rotational constant, its rotational states are far apart, the adiabatic bender curves are well separated, and the method works well. If one applies the method to NO–He, NO–H_2 or O_2–O_2, for example, the much smaller rotational constants of NO and O_2 cause the set of adiabatic bender curves to become rather dense, several avoided crossings occur between them, and the connection to the monomer states is lost.

4.2.4 Analysis of scattering wave functions

With the renormalized Numerov propagator used in the Nijmegen scattering program to solve the CC equations, it is straightforward to generate the scattering wave functions, not only asymptotically but over the full range of R. Thus, one can inspect the character of these wave functions in terms of the participating monomer states and the end-over-end angular momentum l, the partial wave index. If resonance peaks are observed in the ICS, one can determine which total angular momenta J contribute most to these peaks, plot the wave functions for these values of J, and analyze their character. This is illustrated in Fig. 8 for the example of NO–He scattering, already discussed in Sec. 4.2.1, where several resonances were calculated and observed experimentally[47] for collision energies between 13 and 20 cm^{-1}. The wave functions in Fig. 8 contain continuum states, but also have large amplitudes in the region of the well of the NO–He potential, which confirms that they indeed correspond to quasi-bound states. Both resonances shown correspond to the NO state $j = 5/2, f$. Since this channel is open at both resonance energies, they are shape resonances. The resonance at 14.85 cm^{-1} corresponds to $l = 5$, the resonance at 17.75 cm^{-1} to $l = 6$. The excess collision energy is larger for the latter resonance and its continuum contribution is more pronounced, see Fig. 8.

4.2.5 S-matrix Kohn variational method

The **S**-matrix version of the Kohn variational method[78–81,179,180] can also be applied to characterize scattering resonances, as well as to investigate the sensitivity of the resonances to changes in

the PES. For a given J one writes a trial wave function as

$$\widetilde{\psi}_{\mathbf{n},l}(R,\rho) = -\phi_{\mathbf{n},l}(R)\varphi_{\mathbf{n},l}(\rho) + \sum_{\mathbf{n}',l'} \phi^*_{\mathbf{n}',l'}(R)\varphi_{\mathbf{n}',l'}(\rho)\widetilde{S}_{\mathbf{n}',l',\mathbf{n},l} + \sum_k \chi_k(R,\rho)c_k.$$
(57)

The function $\phi_{\mathbf{n},l}(R)$ is an incoming wave at energy $E - \varepsilon_{\mathbf{n}}$, the kinetic energy in channel $\mathbf{n}$, the functions $\phi^*_{\mathbf{n}',l'}(R)$ are the corresponding outgoing waves, and $\widetilde{S}_{\mathbf{n}',l',\mathbf{n},l}$ are the elements of the trial **S**-matrix. The incoming waves, $\phi_{\mathbf{n},l}(R)$, can be chosen freely as long as they satisfy the Schrödinger equation at long range and are regularized at short range. The functions $\chi_k(R,\rho)$ form a bound-state basis. They are eigenfunctions of the Hamiltonian computed with the technique of discrete variable representation (DVR)[181,182] on a finite R-grid and they provide flexibility in the trial wavefunction in the region where $\phi_{\mathbf{n},l}(R)\varphi_{\mathbf{n},l}(\rho)$ does not already solve the Schrödinger equation.

The trial wave function of Eq. (57) is optimized variationally by considering first-order variations with respect to $\widetilde{\mathbf{S}}$ and $\{c_k\}$,

$$\delta\langle\widetilde{\psi}_{\mathbf{n},l}|\hat{H} - E|\widetilde{\psi}_{\mathbf{n},l}\rangle = 2\langle\delta\widetilde{\psi}_{\mathbf{n},l}|\hat{H} - E|\widetilde{\psi}_{\mathbf{n},l}\rangle + i\delta\widetilde{S}_{\mathbf{n},l,\mathbf{n},l}.$$
(58)

The bracket $\langle f|g\rangle = \int_0^\infty dR \int d\rho \, f g$ is defined here without complex conjugation (see a similar trick in Sec. 6.3). An advantage of this approach is that the variational wave function is expressed as a linear combination of a scattering wave function and a set of bound states at short range. Thus, one can analyze which bound state gives rise to a scattering resonance by inspecting the opti-
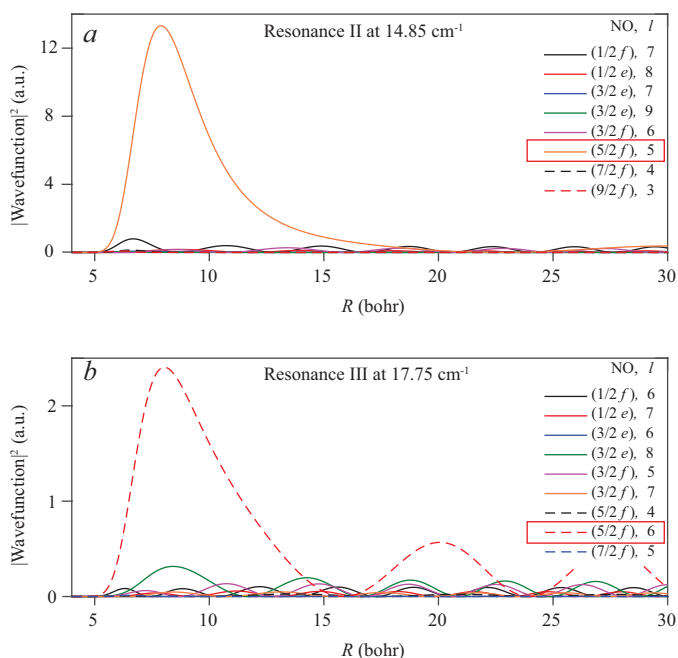

Fig. 8 Scattering wave functions of the NO–He system squared as a function of the distance R. Panel a: At the resonance energy of 14.85 cm^{-1} for $J = 7.5$ and $P = +1$. Panel b: At the resonance energy of 17.75 cm^{-1} for $J = 6.5$ and $P = -1$. The rotational and Λ-doublet state of the NO radical, and the orbital angular momentum of the NO-He complex, are given for each curve. The states that dominate the resonances are marked with a red box. This figure is reproduced from the Supplement of Ref. 47.

mized coefficients $\{c_k\}$.

This method was applied in a combined experimental/theoretical study of NO–He rotationally inelastic scattering at very low collision energies, where resonances are found.[116] The scattering cross sections calculated by the Kohn variational method agree well with those from CC calculations and the assignment of the resonances also agrees with the wave-function analysis described in Sec. 4.2.4. After establishing which quasibound states lead to particular resonances, one can estimate the response of the resonance energies to variations in the PES from the Hellman–Feynman theorem.[183,184] In this way, it was explored how sensitive the resonance energies are to overall scaling of the potential, to scaling of the correlation energy alone, to the anisotropy of the potential, and to a radial shift of the potential.

5 The stabilization method (SM)

We begin the discussion of the various bottom-up approaches with the stabilization method,[84–87,185,186] which has a history of at least 50 years[85] and provides the simplest technique to identify and characterize rovibrational resonances. The stabilization method remains within the realm of variational techniques built upon HQM and L^2 functions. It is important to note right at the start that SM allows the computation of not only resonance positions, ε_n, but also resonance lifetimes, Γ_n^{-1}.[86,187]

5.1 General background

The principal idea behind the SM technique is based on the observation of stabilization of some of the eigenenergies in the (discretized) continuum part of the eigenspectrum of the Hermitian Hamiltonian with respect to (slight) changes in selected computational parameter(s), collectively named τ. During SM computations the size of the basis or the coordinate range on the dissociation coordinate(s) is changed within a narrow interval. The SM techniques differ by how the parameters are selected and how stabilization of certain eigenvalues of the Hermitian Hamiltonian is observed. It is important to emphasize that stabilization of resonances is not an empirical observation but it is based on fundamental properties of basic scattering theory. Stabilization can be understood *via* simple models of isolated resonances. A detailed exposure is given, for example, in Ref. 87.

In the stabilization method we approximate the eigenstates above the dissociation threshold by performing a number of bound-state-type computations with slightly different values for the computational parameter(s), τ. The wave function of a stable resonance state has large amplitudes localized within the interaction region of the fragments; thus, the energy is not sensitive to minor changes in the basis. Contrary to this, the continuum states (a) become "discretized" due to the finite range of the dissociation coordinate, (b) are characterized by wave functions which have significant amplitude outside the deeper region of the potential well, and (c) have energies varying with the coordinate range and the type of the basis used. Thus, due to the large density of continuum states around a resonance, minuscule changes in the basis will yield minuscule change in the resonance energy, while the eigenenergies of continuum states will shift considerably.
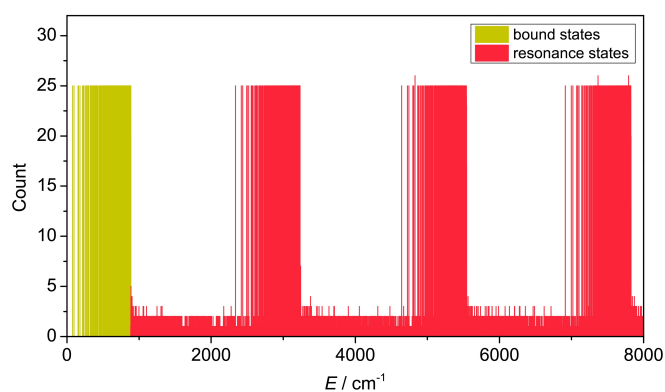

Fig. 9 Overview of the stabilization-method (SM) histogram of Ar·NO$^+$ in the 0–8000 cm^{-1} energy interval based on 25 separate vibrational bound-state (L^2) computations.

The traditional technique to observe resonances through the SM method employs $E_n(\tau)$ stabilization graphs, usually the principal outputs of SM computations. A resonance is observed when a plateau is seen in $E_n(\tau)$, a result of a slowly varying eigenvalue, identified as a resonance position. However, in the large basis limit, the density of states becomes infinite, and no plateau can be observed in $E_n(\tau)$. In this case resonance energies are indicated by inflection points of the $E_n(\tau)$ curves. Another possibility is to compute the expectation value of R^2 ($\langle R^2 \rangle$), where R is a dissociation coordinate. Since $\langle R^2 \rangle$ is much smaller for resonance wave functions than for the discretized continuum states, $\langle R^2 \rangle$ values provide good criteria for the identification of resonances.

In perhaps the simplest form of SM, identification of resonance eigenvalues is achieved using the technique of histogram binning.[64] The TInSE computations are performed for a small number of cases, say 25, with slightly different ranges along the dissociation coordinate. The eigenvalues are collected from all computations, and histograms are generated with a certain bin size. The horizontal axis corresponds to the binned energy scale, while the number of repeated simulations determines the count number on the vertical axis of the histogram (see Fig. 9 for the case of the Ar·NO$^+$ complex with an energy scale of 0–8000 cm^{-1}). As expected, the smaller the bin size the better the performance of the method, a good choice in the case of tightly converged eigenstates is 0.001 cm^{-1}. The stable resonance energies are indicated by peaks on the histogram.

So far the SM technique has not been used in the Budapest group for the determination of resonance lifetimes. This is due to the fact that this requires considerably more computational effort than the determination of the positions. In the experience of the Budapest group, the SM technique is quite successful in identifying long-lived quasibound states. Finding resonances with short lifetime may be difficult though as the energy of these states is considerably more sensitive to computational parameters than those of the long-lived resonances. Furthermore, the CAP-based and CCS techniques are much more appropriate to obtain a large number (if not all) resonances (both positions and lifetimes).

5.2 Application: SM analysis of the vibrational resonances of Ar·NO$^+$

During the study reported in Ref. 64 the SM method was used to identify high-lying vibrational resonance states of the Ar·NO$^+$ complex. In fact, the SM histogram of Fig. 9 represents the computed eigenvalues of the Ar·NO$^+$ complex between 0 and 8000 cm^{-1}.[64] Because the dissociation energy, D_0, of the Ar·NO$^+$ complex is 887 cm^{-1},[64] the states with green color at the left of the figure correspond to bound states. The bound states show a clear and well-defined termination upper limit at D_0. The three further stacks between 2300–3200, 4600–5500, and 6900–7800 cm^{-1} show significant similarity with the stack corresponding to the bound states. They correspond to the first, second, and third excited NO$^+$ stretch states of Ar·NO$^+$ and the width of each stack is approximately D_0 (with a very slight variation). Thus, Fig. 9 can be explained *via* a very simple physical picture: the nearly ideal adiabatic separation of the small-amplitude NO$^+$ stretch motion from the other two, large-amplitude, intermonomer motions.

Pushing the computations to even higher NO$^+$ stretch quantum numbers is hindered by the extremely large number of eigenvalues that would need to be computed variationally. In fact, Fig. 9 is based on the first 12 000 vibrational eigenenergies of the Ar·NO$^+$ system, computed iteratively.[64]

6 The complex absorbing potential (CAP) technique

Complex absorbing, or as sometimes called optical, potentials have been used both in the time-independent and time-dependent formulations of quantum mechanics. The CAP technique[56,88,89,188–193] is probably the most commonly used approach to compute rovibrational resonance states. In the CAP technique the rovibrational Hermitian Hamiltonian is "perturbed" with a complex potential, introduced to absorb the outgoing part of the resonance eigenfunctions, making them square integrable. This approximation to resonance wave functions employs an expansion using an L^2 basis, *e.g.*, the bound states and the eigenstates with energies above dissociation originating from a bound-state computation. Even though CAP-perturbed Hamiltonians act on square-integrable functions, it is not a Hermitian formalism because of the complex potential. Ref. 88 explores the CAP method and its properties with mathematical rigor, while a more general review of the CAP technique can be found in Ref. 89.

6.1 General background

The modified CAP Hamiltonian can be written as

$$\hat{H}'(\eta) = \hat{H} - \mathrm{i}\eta W(R), \tag{59}$$

where $\hat{H}$ is the unperturbed and $\hat{H}'$ is a complex Hamiltonian, η is the CAP-strength parameter, and $W(R)$ is usually a real-valued function of the R dissociation coordinate assuming nonzero values at the asymptotic region of the PES (more than one dissociation coordinate, of course, is also feasible). Complex valued $W(R)$ CAP functions have also been studied.[194]

A useful approach emerges when the CAP-perturbed non-Hermitian Hamiltonian is represented in the basis of the eigenvec-

tors computed with a bound-state code up to and above the first dissociation threshold. Some of the eigenvalues of the complex matrix representation of $\hat{H}'(\eta)$ are approximations to the true resonance energies. The resonance eigenenergies are characterized by two sources of error. The first error is caused by the presence of the CAP function added to the Hamiltonian. This error is small for small η values and large for large η values. The second error is the basis set error, arising because we try to represent a non-square-integrable function with L^2 basis functions. This type of error becomes small for sufficiently large η values, and remains large if the η value is small and the wave function is not damped sufficiently.

To find an optimal η value, where the two types of error either cancel each other out or at least their sum becomes minimal, eigenvalue trajectories in the complex plane need to be generated by varying the CAP-strength parameter. Resonance cusps within the trajectories are then detected and they are associated with an optimal η, yielding resonance positions and lifetimes. Here "cusp" means that there is a sharp bend (local maximum of the curvature) on the trajectory and the density of points has a maximum.

The efficiency of different types of CAP functions has been investigated in a number of studies and various recommendations have been made; see, for example, Refs. 192–198. In our own experience, if the applied L^2 basis set is large enough, then the resonance eigenvalues are not particularly sensitive to the specific form of the CAP function used (as long as the CAP function has significant magnitude in the coordinate ranges, appropriate for absorbing the outgoing part of the wave function).

6.2 GENIUSH-CAP

One implementation of the CAP method for the computation of rotational-vibrational resonance states of arbitrary systems is part of the GENIUSH-CAP code.[65] One needs to perform one expensive bound-state-type computation with the bound-state code GENIUSH,[146,147] which solves TInSE quasi-variationally, in order to compute energies and wave functions above the first dissociation threshold. The GENIUSH eigenvectors are then used as a basis to build the matrix of $\hat{H}'(\eta)$, whose complex eigenvalues are finally computed. Repeating this for a few hundred η values leads to complex eigenvalue trajectories. In the traditional CAP method visual analysis is used to identify resonance cusps in the trajectories.

The CAP approach has several advantages over the stabilization method. First, in the case of the SM technique one needs to perform a few tens of variational bound-state computations, which can take a considerable amount of computer time, while the CAP technique may require only one expensive bound-state computation. Second, the follow-up computation of CAP trajectories is inexpensive, because the matrix of the modified Hamiltonian $\hat{H}'(\eta)$ is *much* smaller than that of the original Hamiltonian, $\hat{H}$. Third, the CAP method is significantly better suited to identify both short- and long-lived resonances.

When compared to the complex coordinate scaling (CCS) technique, see Sec. 7, the CAP technique has another major advan-

tage: the CAP changes only the potential-energy part of the Hamiltonian. Thus, CAP-based techniques do not require the knowledge of the Hamiltonian in an analytic form and the CAP technique can be incorporated straightforwardly into numerical techniques based upon the discrete variable representation [181,182] of the Hamiltonian. This is exactly why we decided to extend our fourth-age quantum-chemical [83] code GENIUSH, [146,147] built upon the DVR representation of the Hamiltonian, with the CAP capability.

The only considerable drawback of the CAP method is the need for visual searches for cusps. This takes a lot of human effort, and introduces some subjectivity to the collection of resonance states. There have been some reports about automatic cusp recognition, *e.g.*, the method of Silva *et al.*[62] There the cusps are identified based on the curvature of the CAP trajectories and the density of the points. In our experience it is easy to either miss rovibrational resonances or to assign false positives this way. Thus, we considered another approach for automating CAP computations, named the extended Tremblay–Carrington (ETC) method,[61,68] discussed in the next subsection.

6.3 The ETC method

The principal advantage of the ETC method[68] is that it makes the computation of rovibrational resonance states automatic. Using the ETC method the resonance energies are obtained as eigenvalues of an unmodified Hamiltonian matrix built in a suitable basis, which is composed of selected eigenvectors of a CAP computation. This way one completely circumvents the computation of CAP trajectories.

The algorithm of the ETC method is as follows. First, solve a CAP-type eigenvalue equation with a suitable CAP-strength pa-

rameter, η_{guide},

$$\hat{H}'(\eta_{\text{guide}})|\phi_k\rangle = (\hat{H} - i\eta_{\text{guide}}W(R))|\phi_k\rangle = E_k|\phi_k\rangle. \quad (60)$$

This step can be performed, among others, with the GENIUSH-CAP code.[65] Second, select carefully a basis set $\{|\phi_k\rangle\}$ from the eigenvectors obtained in step (1). This is a very important step as one must choose only those eigenvectors which became square-integrable due to the CAP, *i.e.*, they are small where the CAP function is large. As shown in Ref. 68, selection of the basis $\{|\phi_k\rangle\}$ can be done more or less automatically, based on the complex eigenvalues E_k. The basis functions are normalized such that $\langle \phi_k^*|\phi_l\rangle = \delta_{kl}$, contrary to the conventional normalization $\langle \phi_k|\phi_l\rangle = \delta_{kl}$. Third, one builds the matrix of the original Hamiltonian in this basis,

$$H_{kl} = \langle \phi_k^*|\hat{H}|\phi_l\rangle, \quad (61)$$

and solves the eigenvalue equation. The Hamiltonian matrix built this way is clearly not Hermitian and thus it has complex eigenvalues. Furthermore, there are more basis functions than resonances. In order to identify which complex eigenvalues belong to resonance states, we repeat the three steps described, with a few (let's say 11) slightly different η_{guide} values. The resonance eigenvalues are less sensitive to the choice of η_{guide} than the ones that do not correspond to resonance states. If we plot the computed eigenenergies resulting from all η_{guide} values on the complex plane, they form well-defined clusters. The points within a cluster belong to the same state but they are obtained with different η_{guide} values. Eigenvalues corresponding to resonance states form compact clusters, while the non-resonance eigenvalues form clusters that are considerably more extended. In order to make this approach automatic, clusters must be characterized by suitable algorithms facilitating their observation. For a suitable choice of a scoring algorithm Ref. 68 should be consulted, in which appraisal scores are assigned to each cluster to guide the selection of resonance states.

Because the computations following the usually expensive bound-state computation are inexpensive, due to the small size of the Hamiltonian matrix built with the carefully selected $\{|\phi_k\rangle\}$ basis, the additional computations with different η_{guide} values do not increase the overall cost of the determination of rovibrational resonances *via* the ETC method at all.

6.4 Applications

6.4.1 Vibrational resonances of Ar·NO$^+$

In Ref. 64, not only the SM but also a CAP-based method (and a scattering method, see above) was used to identify and characterize the resonance states of the Ar·NO$^+$ complex. The long-lived resonance states found by the SM method (see Fig. 10) have been confirmed by the GENIUSH-CAP method as states with long lifetimes when compared to the other resonance states in their vicinity.

Fig. 11 shows a few selected GENIUSH-CAP eigenvalue trajectories with various forms of cusps. The three different colors indicate the different basis set sizes along the Ar–NO$^+$ distance used in the bound-state-type GENIUSH computation, thereby reflect-
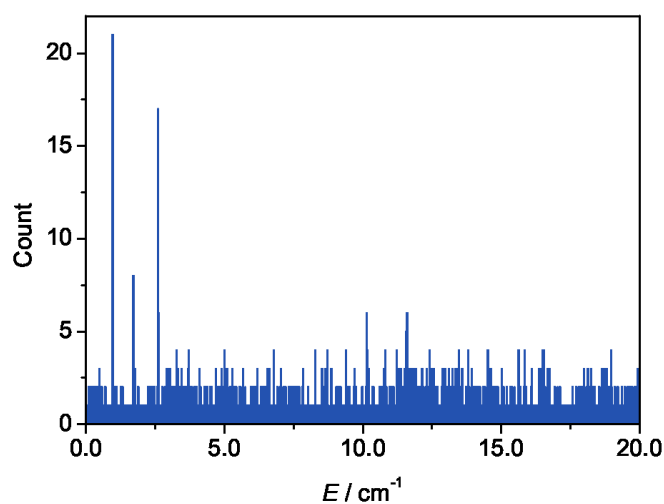

Fig. 10 Stabilization-method (SM) histogram of Ar·NO$^+$, with a bin size of 0.01 cm^{-1}, within the energy range 20 cm^{-1} above the first dissociation limit, D_0(ArNO$^+$)=887 cm^{-1}. Eigenvalues are obtained from 25 GENIUSH computations.

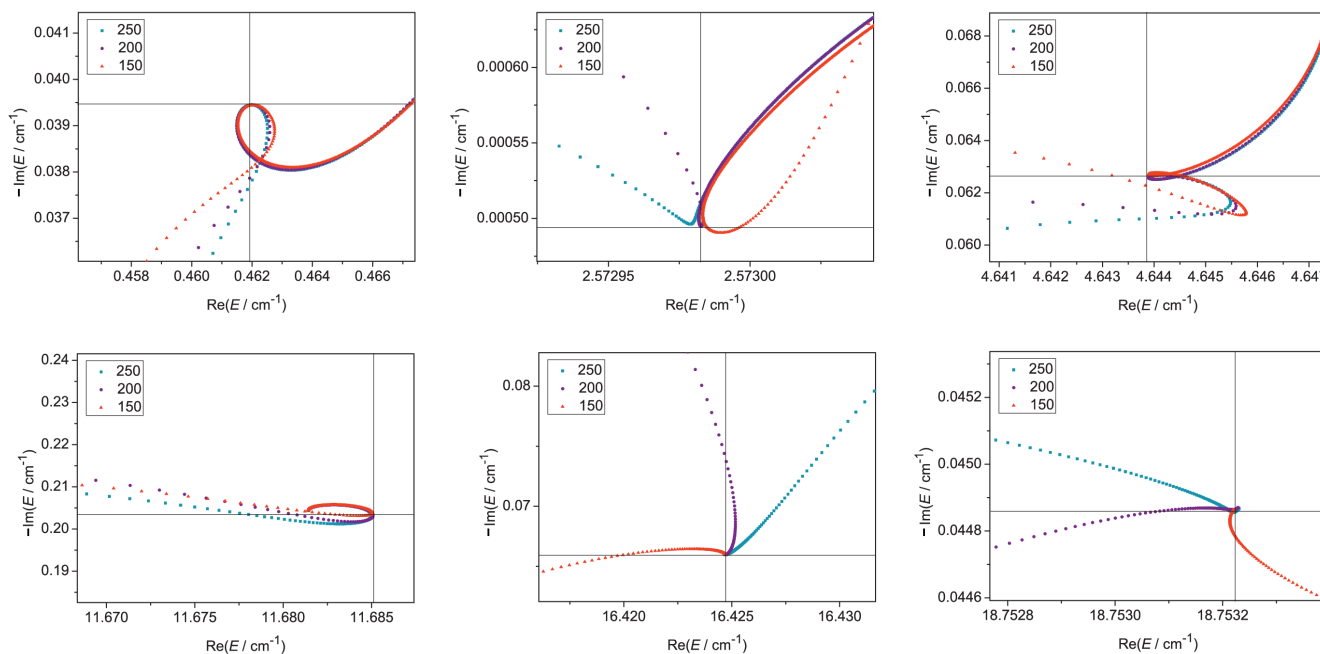**Fig. 11** GENIUSH-CAP eigenvalue trajectories in the vicinity of six selected resonances of Ar·NO$^+$ in the energy region above the first dissociation threshold. Zero energy is taken as the energy of the separated Ar and NO$^+$($v = 0, j = 0$) systems. The CAP eigenvalue trajectories are obtained using three different computations performed with 150, 200, and 250 DVR points along the R dissociation coordinate (Ar$\cdots$NO$^+$), reflecting the convergence of the resonance energies and lifetimes. In each panel, the points of intersection of the vertical and horizontal lines point out the cusps in the trajectories.

ing graphically the convergence of the resonance energies and lifetimes.

6.4.2 Vibrational resonances of H$_2$·CO

In Ref. 65, the vibrational resonances of the weakly-bound complex H$_2$·CO were computed using the GENIUSH-CAP approach and a four-dimensional model PES. Thus, this is one of the few cases where reduced-dimensional resonance treatments have been reported for a vdW complex.

Resonances of both *para-* and *ortho-*H$_2$·CO were identified and characterized with the help of the computations. Quantum-number assignments for the resonances were achieved by inspecting the vibrational probability density plots and by computing wave function overlaps with eigenstates of reduced-dimensional models.

6.4.3 Rotational-vibrational resonances of (H$_2$)$_2$

Computation of the rovibrational resonances of (H$_2$)$_2$ served as a test of the ETC method, [68] described in Sec. 6.3. (H$_2$)$_2$ is a very weakly-bound vdW complex, its dissociation threshold is only about $D_0((H_2)_2) = 3$ cm^{-1}. The rotational constant of the H$_2$ molecule is approximately 60 cm^{-1}, larger than the dissociation energy. Therefore, if either of the two H$_2$ monomers is in a rotationally excited state, the energy of the dimer exceeds the lowest dissociation threshold. Thus, there is a large number of shape and Feshbach-type rovibrational resonances for (H$_2$)$_2$. In fact, only the ground state of the intermonomer stretch is bound, and there are multiple dissociation channels corresponding to the different rotational states of the H$_2$ monomers. Both bound and

resonance states are located near each dissociation channel, in which the H$_2$ molecules are rotationally excited.

The computations of Ref. 68 revealed some extremely long-lived resonance states, whose energy is lower than the dissociation threshold corresponding to the rotational state of the monomers. These states dissociate into a symmetry-accessible lower-lying dissociation channel. These resonances are very similar to bound states, and their very long lifetime cannot be determined precisely.

There are short-lived resonances whose energy is larger than the dissociation limit corresponding to the rotational state of the monomers. These states were determined using both the ETC and the GENIUSH-CAP methods. The two techniques resulted in very similar resonances. The ETC method proved to be an outstanding and automatic alternative to the original CAP method.

6.5 Comparison of GENIUSH-CAP and scattering results for Ar·NO$^+$

Since in Ref. 64 both the CC Hermitian scattering and a non-Hermitian CAP methods were utilized to compute vibrational resonance states for Ar·NO$^+$, it is worth discussing the relation of the results obtained with the two different approaches.

Although there are several reasons why the comparison between the resonance states obtained *via* the CAP and CC computations of Ref. 64 is not straightforward, it was found that the two basically different approaches provide results in good agreement not only for the bound but also for the resonance states: all significant CC resonance peaks could be paired with a CAP res-
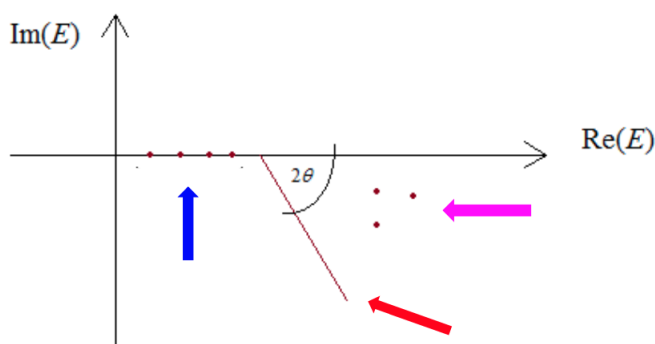
Fig. 12 Illustration of the eigenvalues of a complex-scaled Hamiltonian in the vicinity of one dissociation channel. The blue and purple arrows point out the bound and resonance eigenvalues, respectively, while the red arrow points out the rotated scattering continuum.

onance within a few 0.1 cm^{-1} (the expected agreement of the results obtained with the two techniques). The lifetimes obtained as the eigenvalues of the close-coupling Smith lifetime matrix and GENIUSH-CAP lifetimes also showed reasonable agreement for the longer-lived resonances.

7 The complex coordinate scaling (CCS) method

7.1 General background

In the non-Hermitian CCS scheme rovibrational resonance states are computed as the exponentially diverging solutions of the TInSE, see Eq. (50). Within the CCS scheme one introduces an invertible operator $\hat{S}$, so that the functions $\Phi_n = \hat{S}\Psi_n^{res}$ become square integrable. The similarity-transformed Schrödinger equation reads as

$$\hat{S}\hat{H}\hat{S}^{-1}\Phi_n = E_n^{res}\Phi_n, \ \Phi \in L^2. \tag{62}$$

Eq. (62) is an eigenvalue equation for the transformed Hamiltonian $\hat{S}\hat{H}\hat{S}^{-1}$, whereby the eigenfunctions are square integrable and the eigenvalues are the desired resonance eigenenergies. Eq. (62) can be solved with the well-developed L^2 techniques of quantum chemistry.

In the conventional CCS method, a choice for the operator $\hat{S}$ is

$$\hat{S}_\theta f(R) = f(Re^{i\theta}), \tag{63}$$

where θ is a free parameter and R is the dissociation coordinate. Therefore, the operator $\hat{S}_\theta$ rotates the argument of a function of the dissociation coordinate by θ in the complex plane. If there is more than one dissociation coordinate, each should undergo a complex coordinate scaling transformation. Due to the transformation by $\hat{S}_\theta$,[77,90–92,96,97] (a) resonance states for which $2\theta > \arctan(\Gamma/(2(\varepsilon - D_0))) = \text{Arg}(E^{res} - D_0)$ will become square integrable, (b) bound states remain square integrable for $\theta < \pi/4$ (which is true in all practical applications), and (c) the scaled Hamiltonian has scattering eigenfunctions which are associated with a continuum that is rotated into the lower half of the complex energy plane by the angle 2θ.[91,92,96,97] Thus, in the spectrum of the scaled Hamiltonian of Eq. (62), (a) real discrete

eigenvalues (unaffected by the CCS) correspond to bound states, (b) the scattering continuum is rotated into the lower half of the complex plane by 2θ for each dissociation channel, and (c) discrete complex eigenvalues in the area between the real axis and the rotated scattering continua correspond to resonance states, see Fig. 12.

Obtaining the form of the scaled Hamiltonian is rather straightforward in the case of conventional complex scaling. For differential operators corresponding to the dissociation coordinate R, one needs to make the change $\frac{\partial}{\partial R} \to \frac{\partial}{\partial R}e^{-i\theta}$. For operators depending only on the coordinate the change $R \to Re^{i\theta}$ is required.[96,97] In its simplest form, CCS requires a PES that can be evaluated at complex coordinate values, which can be achieved for PESs having a fitted analytical form, once one rewrites the PES subroutine into complex arithmetic. In addition, various techniques, also applicable for non-analytical PESs, are available; for examples, see Refs. 98, 199, and 200.

Somewhat more involved but often more convenient and numerically more efficient extensions of the CCS method have been developed. These include the method of exterior complex scaling,[201,202] whereby the transformation is defined, for $R \geq R_s$, as

$$\hat{S}_\theta f(R) = f(R_s + e^{i\theta}(R - R_s)). \tag{64}$$

The exterior complex scaling transformation has been implemented for grid-based techniques,[203,204] and a smooth exterior complex scaling method[73] has also been advocated. Note that the CAP method can be derived from smooth exterior complex scaling by applying certain approximations.[73,205]

Naturally, resonance eigenenergies with a physical meaning should be independent of the scaling parameter θ in Eq. (63). However, in practice, when finite basis sets are used, the form of the Φ_n eigenfunctions and thus the "goodness" of the basis depends on the scaling parameter. Similar to the CAP method, resonance eigenenergies can be identified in the CCS formalism by locating stationary points in eigenvalue trajectories obtained by varying the scaling parameter θ.

7.2 Applications
7.2.1 Rotational-vibrational resonances of $H_2{}^{16}O$

$H_2{}^{16}O$ is a strongly-bound molecule for which rovibrational resonance states have been identified experimentally.[12] Therefore, performing rovibrational resonance computations for this species is extremely important to test the utility of the different techniques. In Ref. 13 the spectrum of $H_2{}^{16}O$ was simulated above the first dissociation threshold using advanced electronic structure and nuclear motion computations, and the simulated spectrum was compared to the experimental one from Ref. 12. Several Feshbach and shape resonances were determined with the CAP method, and a broad spectral feature resulting from the direct photodissociation to the continuum was also revealed in this study.

In Ref. 14 the low-lying rovibrational resonances of $H_2{}^{16}O$ were computed using the CCS method. During these calculations the matrix representation of the scaled Hamiltonian was obtained in
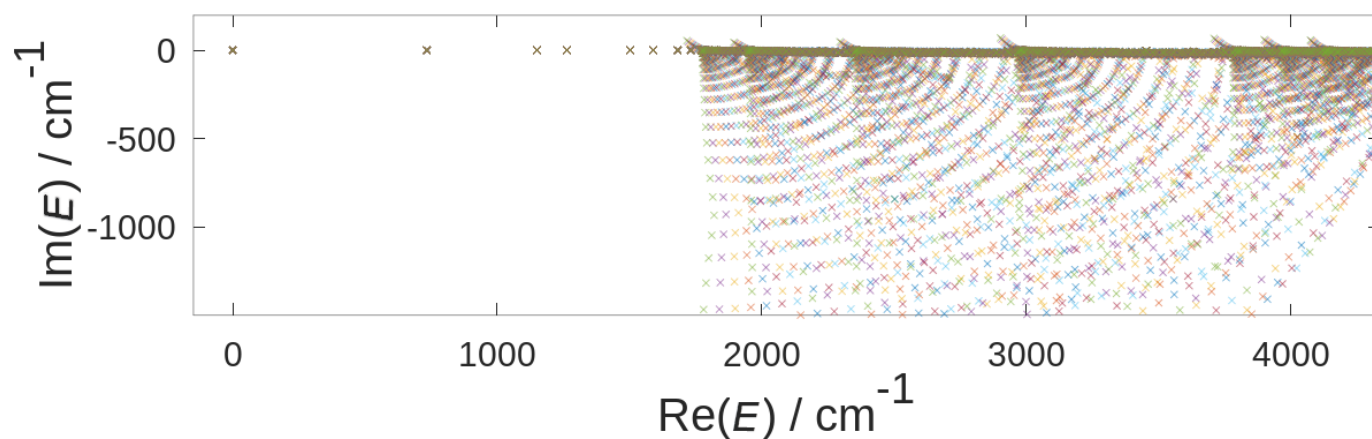
Fig. 13 Eigenvalue trajectories of H_2He^+ on the complex energy plane, obtained by varying the scaling parameter of the complex coordinate scaling (CCS) method between 0.02 and 0.80 in 40 steps. See Ref. 67 for computational details.

two steps. First, all the bound states of the unscaled Hamiltonian were computed, using the code D^2FOPI, [104] along with many eigenpairs having energies above the dissociation threshold. In the second step, using a subset of the computed eigenvectors as an orthonormal basis set, the matrix of the scaled Hamiltonian was constructed,

$$\mathbf{H}_{kl}^{\theta} = \langle \Psi_k | \hat{S}_\theta \hat{H} \hat{S}_\theta^{-1} | \Psi_l \rangle, \tag{65}$$

resulting in a matrix with modest size, on the order of around a thousand-by-thousand, which could be directly diagonalized for the few dozen θ values required to form the complex eigenvalue trajectories. Inspection of the vibrational probability density plots from the stationary resonance calculations revealed several types of (dynamical) dissociation behavior, varying among the states. The calculations aided the proper assignment of some observed rovibrational transitions beyond the first dissociation threshold of $H_2{}^{16}O$. [13]

7.2.2 Rotational-vibrational resonances of H_2He^+

In Ref. 67, a large number of rovibrational resonances has been computed and characterized for the H_2He^+ molecular ion, using the CCS, the CAP, and the SM techniques. These accurate computations of the bound and resonance states facilitate the first experimental observation of rovibrational transitions of this fundamental molecule, made up of the two most abundant elements of the universe. The CCS algorithm employed was basically the same as that detailed for $H_2{}^{16}O$ in the previous subsection. Fig. 13 shows some CCS eigenvalue trajectories computed in Ref. 67, reflecting a number of dissociation channels, corresponding to the different rotational states of the H_2^+ moiety in the dissociated system.

Beyond the spectroscopic data, valuable for future high-resolution experiments, the quantum-chemical computations on H_2He^+ also revealed dissociation pathways, dissociation branching ratios, and the stabilization mechanism of the long-lived resonances. Because the H–H stretching fundamental lies above the first dissociation threshold of H_2He^+, $D_0(H_2He^+) = 1775.4$ cm^{-1},

resonances are expected to play a crucial role in the collision and association reactions involving H_2He^+, including radiative association and radiative charge-transfer reactions. Fig. 14 shows the probability density plot of a selected vibrational resonance of H_2He^+, computed in Ref. 67. The resonance shown in Fig. 14 is a Feshbach resonance, in which the H_2^+ moiety is rotationally highly excited in the interaction region.
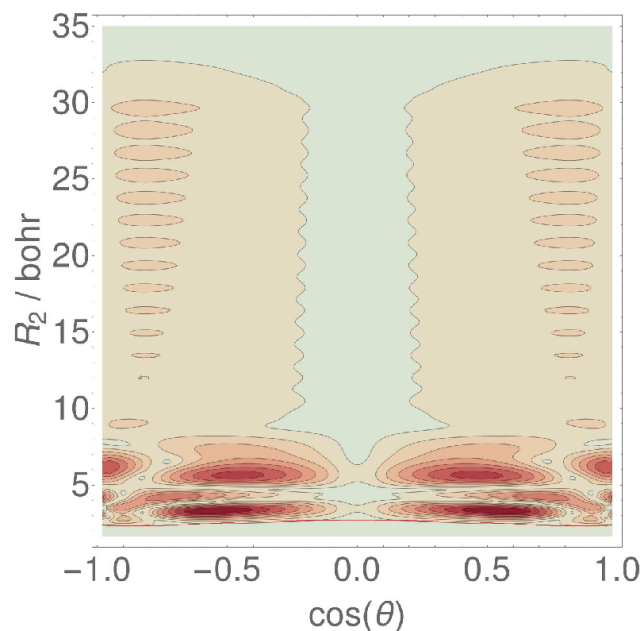

Fig. 14 The nodal structure of a $J = 0$ vibrational resonance state of H_2He^+ located at around 2109.4 cm^{-1} above its zero-point vibrational energy, where R_2 and θ denote the H_2^+−He distance and the Jacobi angle defined by the H_2^+−He and H−H bonds, respectively. See Ref. 67 for computational details.

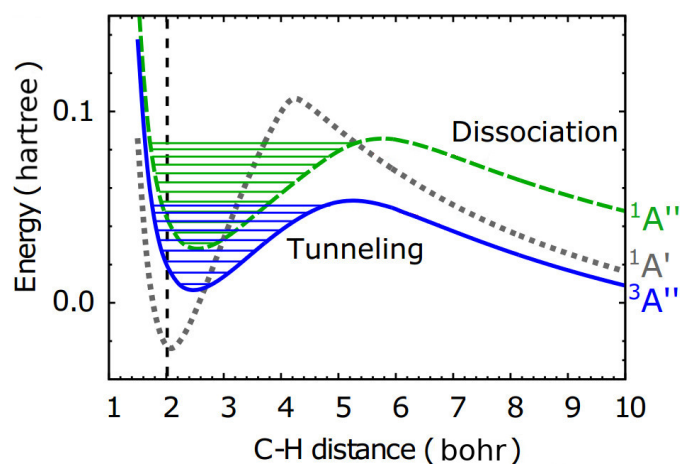**Fig. 15** Calculated potential energy curves along a C−H stretching coordinate of the planar ethylene dication, $C_2H_4^+$. The gray dotted line shows the electronic ground state, while the blue solid line and the green dashed line correspond to the first and second electronically excited states, respectively. Horizontal lines represent vibrational states. See Ref. 206 for computational details.

7.2.3 Understanding the ultraslow decay in Coulomb explosion of hydrocarbons

In the experiments described in Ref. 206, the $C_2H_2^{2+}$ and $C_2H_4^{2+}$ dications were generated by double ionization with few-cycle intense laser pulses. In the deprotonation pathway of the Coulomb explosion for both $C_2H_2^{2+}$ and $C_2H_4^{2+}$, an ultraslow, microsecond timescale exponential decay channel was observed.

Reduced-dimensional resonance-state computations,[206] utilizing the CCS method, revealed that in both cases the slow decay channel is due to quasibound states along the C–H vibrational mode, where tunneling through a barrier is responsible for the exponential decay, see Fig. 15.

8　Summary and outlook

The extremely rich internal dynamics of molecular systems just below and above the first dissociation threshold can be studied with a variety of quantum-chemical bound, resonance, and scattering techniques employing accurate potential energy surfaces, corresponding usually to the ground electronic state and exhibiting correct asymptotic behavior. This Perspective focuses on the first-principles computation and characterization of rovibrational resonances, proving that, depending on the chemistry, getting together or breaking up are complex processes even for molecular systems.

Most rovibrational resonance states can be categorized based on their physical origin, they can be shape or Feshbach-type resonances. One can approach resonance states either from the direction of bound states (a bottom-up approach) or from scattering states (a top-down approach). Next, we concentrate first on the bottom-up and then on the top-down first-principles approaches. Then we give some information about experiments related to rovibrational resonance states.

The complex algorithms and codes developed for bound-state computations during the fourth age of quantum chemistry are suitable to determine and describe the numerous L^2 bound rovibrational states. As to resonances, the stabilization method (SM) allows the utilization of bound-state computations to determine long-lived resonances (both their position and lifetime). The SM method is based on the fact that the eigenenergies of a Hermitian Hamiltonian corresponding to resonances are rather insensitive to slight changes in certain parameters of the bound-state-type computation. Thus, if one can perform a considerable number of bound-state computations yielding a large number of unbound states, a histogram binning approach can be utilized to identify long-lived resonances among the unbound states in a straightforward manner.

Apart from the simple "trick" of repeating them many times, bound-state variational approaches are unsuitable for the computation of resonances without appropriate modifications. There are two basic routes one can take, both are based on the regularization of the diverging resonance wave functions. In the case of the complex absorbing potential (CAP) method, the outgoing part of the wave function is damped by a complex potential added to the molecular PES along the dissociative mode(s). The CAP ensures that resonance wave functions can be expanded in an L^2 basis. A variant of the CAP methods, the extended Tremblay–Carrington (ETC) scheme allows an almost automatic (black-box-type) determination of rovibrational resonances. Since the ETC method can be coupled to the best general-purpose solvers of the time-independent nuclear Schrödinger equation, the resulting algorithm and code is available to compute rovibrational resonances of larger systems, perhaps in reduced dimension, in a semi-automatic way.

The alternative complex coordinate scaling (CCS) technique involves a complex coordinate transformation along the dissociation degree of freedom. Most variants of this technique require the availability of the Hamiltonian, including the PES, in an analytic form, which is usually not a significant restriction.

Variants of the SM, the CAP, and the CCS techniques have been successfully applied by members of the Budapest group for several small systems, such as triatomic molecules (the strongly-bound $H_2^{16}O$ and H_2He^+), atom-diatom complexes ($Ar·NO^+$), diatom-diatom complexes ($H_2·CO$ and $(H_2)_2$), and small cationic systems ($C_2H_2^{2+}$ and $C_2H_4^{2+}$).

The scattering problem can also be solved using different first-principles techniques. The coupled-channels (or sometimes called close-coupling) technique employs a Hermitian Hamiltonian and a coupled-channel basis corresponding to the different quantum states of the colliding molecules and products. The coupled-channels equations are solved by numerical integration. In the case of the Kohn variational method the trial wave function, which contains both scattering basis functions and bound state basis functions, is optimized variationally. Sometimes the adiabatic-bender model is applicable to simplify the scattering problem. This is achieved by separating the radial motion from the rotation and vibration of the colliding molecules. Solving the scattering problem results in the scattering matrix and state-to-state integral and differential cross sections. By analyzing the energy-dependent elements of the scattering matrix, one can sep-

arate the contribution of the resonances from the contribution of the background. Resonances can be characterized either by the complex poles of the scattering matrix, peaks of the integral scattering cross section, or the sharp increase of the phase shift by π as a function of energy. These scattering computations have been employed to investigate the resonances in systems such as NH_3–He, NH_3–H_2, NO–He, NO–H_2, OH–He, OH–Ne, and H_2–He*.

Several techniques which can yield experimental information about rotational-vibrational resonances are available. There is a plethora of crossed molecular beam experiments, starting in the 1960s,[207] which are able to yield detailed results about resonances. Depending upon its resolution, photoelectron velocity-map imaging spectroscopy may provide spectra with a wealth of information about Feshbach resonances. Scattering experiments are becoming increasingly sophisticated, as state-selective preparation of reactants, state-resolved detection of products, as well as velocity and angle resolution of both reactants and products are more and more feasible. As the computational tools for describing rovibrational resonances of polyatomic molecules become ever more efficient and sophisticated, they are expected to play an increasing role in supporting the high-resolution spectroscopy of molecules near and above their dissociation threshold, the experimental efforts in molecular dynamics, including those induced by strong fields, as well as ever more complex scattering experiments.

Finally, we mention that Feshbach resonances may play a role in at present exotic applications, such as the production of (molecular) Bose–Einstein condensates.[208] As explained in the Introduction, it is important for this application that resonances in ultracold collisions can be manipulated with external electric and/or magnetic fields. The manipulation of resonances by external electric and magnetic fields is also of more general interest, since it may open up new possibilities to steer the outcome of reactive and non-reactive collisions, photochemical reactions, unimolecular decay, etc., as shown for model systems and realistic systems alike; see, for example, Refs. 209–213. Crossed molecular beam studies of low-energy molecule-molecule collisions in external fields to explore these possibilities are being prepared.[214] Some related preliminary calculations have already been performed.[215–218]

Conflicts of interest

There are no conflicts of interest to declare.

Acknowledgements

References

1 G. Gamow, *Z. Phys.*, 1928, **51**, 204–212.

2 O. K. Rice, *J. Chem. Phys.*, 1933, **1**, 375–389.

3 U. Fano, *Nuovo Chim.*, 1935, **12**, 154–161.

4 G. Breit and E. P. Wigner, *Phys. Rev.*, 1936, **49**, 519–531.

5 A. F. J. Siegert, *Phys. Rev.*, 1939, **56**, 750–752.

6 H. Feshbach, *Ann. Phys.*, 1958, **5**, 357–390.

7 C. Mahaux, in *Lecture Notes in Physics*, ed. S. Albeverrio, L. S. Ferreia and L. Streit, Springer-Verlag, Berlin, 1984, vol. 211.

8 H. Feshbach, *Theoretical Nuclear Physics: Nuclear Reactions*, Wiley, New York, 1992.

9 L. Fonda and R. G. Newton, *Ann. Phys.*, 1960, **10**, 490–515.

10 M. Qiu, Z. Ren, L. Che, D. Dai, S. A. Harich, X. Wang, X. Yang, C. Xu, D. Xie, M. Gustafsson, R. T. Skodje, Z. Sun and D. H. Zhang, *Science*, 2006, **311**, 1440–1443.

11 D. H. Zhang and H. Guo, *Annu. Rev. Phys. Chem.*, 2016, **67**, 135–158.

12 M. Grechko, P. Maksyutenko, T. R. Rizzo and O. V. Boyarkin, *J. Chem. Phys.*, 2010, **133**, 081103.

13 N. F. Zobov, S. V. Shirin, L. Lodi, B. C. Silva, J. Tennyson, A. G. Császár and O. L. Polyansky, *Chem. Phys. Lett.*, 2011, **507**, 48–51.

14 T. Szidarovszky and A. G. Császár, *Mol. Phys.*, 2013, **111**, 2131–2146.

15 B. K. Kendrick, L. Jayasinghe, S. Moser, M. Auzinsh and N. Shafer-Ray, *Phys. Rev. Lett.*, 2000, **84**, 4325–4328.

16 G. C. Schatz, *Science*, 2000, **288**, 1599–1600.

17 M. L. Weichman, J. A. DeVine, M. C. Babin, J. Li, L. Guo, J. Ma, H. Guo and D. M. Neumark, *Nat. Chem.*, 2017, **9**, 950–955.

18 S. A. Reid and H. Reisler, *Annu. Rev. Phys. Chem.*, 1996, **47**, 495–525.

19 G. J. Schulz, *Phys. Rev. Lett.*, 1963, **10**, 104–105.

20 J. R. Taylor, *Scattering Theory*, Wiley, New York, 1972.

21 J.-M. Hartmann, C. Boulet and D. Robert, *Collisional Effects on Molecular Spectra*, Elsevier, 2008.

22 W. G. Brown and G. E. Gibson, *Phys. Rev.*, 1932, **40**, 529–543.

23 J. M. Hutson, C. J. Ashton and R. J. Le Roy, *J. Phys. Chem.*, 1983, **87**, 2713–2720.

24 M. Okamura, L. I. Yeh and Y. T. Lee, *J. Chem. Phys.*, 1985, **83**, 3705–3706.

25 C. J. Ashton, M. S. Child and J. M. Hutson, *J. Chem. Phys.*, 1983, **78**, 4025–4039.

26 U. Fano, *Phys. Rev.*, 1961, **124**, 1866–1878.

27 W. Domcke, *Phys. Rep.*, 1991, **208**, 97–122.

28 R. Schinke, *Photodissociation Dynamics*, Cambridge University Press, Cambridge, 1993.

29 H. M. Yin, S. H. Kable, X. Zhang and J. M. Bowman, *Science*, 2006, **311**, 1443–1446.

30 K. M. Jones, E. Tiesinga, P. D. Lett and P. S. Julienne, *Rev. Mod. Phys.*, 2006, **78**, 483–535.

31 T. Köhler, K. Góral and P. S. Julienne, *Rev. Mod. Phys.*, 2006,

78, 1311–1361.

32 D. W. Chandler, *J. Chem. Phys.*, 2010, **132**, 110901.

33 Y. Wang and P. S. Julienne, *Nat. Phys.*, 2014, **10**, 768–773.

34 N. Balakrishnan, *J. Chem. Phys.*, 2016, **145**, 150901.

35 R. N. Zare, *Science*, 2006, **311**, 1383–1385.

36 A. Schutte, G. Scoles, F. Tommasini and D. Bassi, *Phys.Rev. Lett.*, 1972, **29**, 979–982.

37 A. Schutte, D. Bassi, F. Tommasini and G. Scoles, *J. Chem. Phys.*, 1975, **62**, 600–605.

38 J. P. Toennies, W. Welz and G. Wolf, *J. Chem. Phys.*, 1974, **61**, 2461–2462.

39 J. P. Toennies, W. Welz and G. Wolf, *J. Chem. Phys.*, 1976, **64**, 5305–5307.

40 J. P. Toennies, W. Welz and G. Wolf, *J. Chem. Phys.*, 1979, **71**, 614–642.

41 R. E. Wyatt and M. J. Redmon, *Chem. Phys. Lett.*, 1983, **96**, 284–288.

42 P. Maksyutenko, T. R. Rizzo and O. V. Boyarkin, *J. Chem. Phys.*, 2006, **125**, 181101.

43 S. Chefdeville, T. Stoecklin, A. Bergeat, K. M. Hickson, C. Naulin and M. Costes, *Phys. Rev. Lett.*, 2012, **109**, 023201.

44 S. Chefdeville, Y. Kalugina, S. Y. T. van de Meerakker, C. Naulin, F. Lique and M. Costes, *Science*, 2013, **341**, 1094–1096.

45 A. B. Henson, S. Gersten, Y. Shagam, J. Narevicius and E. Narevicius, *Science*, 2012, **338**, 234–238.

46 E. Lavert-Ofir, Y. Shagam, A. B. Henson, S. Gersten, J. Kłos, P. S. Żuchowski, J. Narevicius and E. Narevicius, *Nat. Chem.*, 2014, **6**, 332–335.

47 S. N. Vogels, J. Onvlee, S. Chefdeville, A. van der Avoird, G. C. Groenenboom and S. Y. T. van de Meerakker, *Science*, 2015, **350**, 787–790.

48 T. Yang, J. Chen, L. Huang, T. Wang, C. Xiao, Z. Sun, D. Dai, X. Yang and D. H. Zhang, *Science*, 2015, **347**, 60–63.

49 A. Bergeat, J. Onvlee, C. Naulin, A. van der Avoird and M. Costes, *Nat. Chem.*, 2015, **7**, 349–353.

50 M. Beyer and F. Merkt, *Phys. Rev. Lett.*, 2016, **116**, 093001.

51 A. Klein, Y. Shagam, W. Skomorowski, P. S. Żuchowski, M. Pawlak, L. M. C. Janssen, N. Moiseyev, S. Y. T. van de Meerakker, A. van der Avoird, C. P. Koch and E. Narevicius, *Nat. Phys.*, 2017, **13**, 35–38.

52 J. Zou, S. D. S. Gordon, S. Tanteri and A. Osterwalder, *J. Chem. Phys.*, 2018, **148**, 164310.

53 S. D. S. Gordon, J. J. Omiste and A. Osterwalder, *Nat. Chem.*, 2018, **10**, 1190–1195.

54 C. Amarasinghe, H. Li, C. A. Perera, M. Besemer, A. van der Avoird, G. C. Groenenboom, C. Xie, H. Guo and A. G. Suits, *J. Phys. Chem. Lett.*, 2019, **10**, 2422–2427.

55 C. Amarasinghe, H. Li, C. A. Perera, M. Besemer, A. van der Avoird, G. C. Groenenboom, J. Zuo, C. Xie, H. Guo, J. Kłos and A. G. Suits, *Nat. Chem.*, 2020, **accepted**,.

56 D. Wang and J. M. Bowman, *J. Chem. Phys.*, 1994, **100**, 1021–1027.

57 H.-J. Werner, C. Bauer, P. Rosmus, H.-M. Keller, M. Stumpf and R. Schinke, *J. Chem. Phys.*, 1995, **102**, 3593–3611.

58 V. Ryaboy and N. Moiseyev, *J. Chem. Phys.*, 1995, **103**, 4061–4068.

59 V. A. Mandelshtam and H. S. Taylor, *J. Chem. Phys.*, 1997, **106**, 5085–5090.

60 B. Poirier and T. Carrington Jr., *J. Chem. Phys.*, 2002, **116**, 1215–1227.

61 J. Tremblay and T. Carrington, *J. Chem. Phys.*, 2005, **122**, 244107.

62 B. C. Silva, P. Barletta, J. J. Munro and J. Tennyson, *J. Chem. Phys.*, 2008, **128**, 244312.

63 K. B. Gubbels, Q. Ma, M. Alexander, P. Dagdigian, D. Tanis, G. C. Groenenboom, A. van der Avoird and S. Y. T. van de Meerakker, *J. Chem. Phys.*, 2012, **136**, 144308.

64 D. Papp, J. Sarka, T. Szidarovszky, A. G. Császár, E. Mátyus, M. Hochlaf and T. Stoecklin, *Phys. Chem. Chem. Phys.*, 2017, **19**, 8152–8160.

65 D. Papp, T. Szidarovszky and A. G. Császár, *J. Chem. Phys.*, 2017, **147**, 094106.

66 S. N. Vogels, T. Karman, J. Kłos, M. Besemer, J. Onvlee, A. van der Avoird, G. C. Groenenboom and S. Y. T. van de Meerakker, *Nat. Chem.*, 2018, **10**, 435–440.

67 D. Papp, A. G. Császár, K. Yamanouchi and T. Szidarovszky, *J. Chem. Theory Comput.*, 2018, **14**, 1523–1533.

68 I. Simkó, T. Szidarovszky and A. G. Császár, *J. Chem. Theory Comput.*, 2019, **15**, 4156–4169.

69 L. D. Landau and E. M. Lifshitz, *Quantum Mechanics, 3rd ed.*, Pergamon, Oxford, 1977.

70 R. McWeeny, *Methods of Molecular Quantum Mechanics*, Academic Press, London, 1992.

71 J. von Neumann, *Mathematical Foundations of Quantum Mechanics*, Princeton University Press, Princeton, 1997.

72 C. M. Bender, *Rep. Prog. Phys.*, 2007, **70**, 947–1018.

73 N. Moiseyev, *Non-Hermitian Quantum Mechanics*, Cambridge University Press, Cambridge, 2011.

74 E. J. Brändas, *Adv. Quant. Chem.*, 2012, **63**, 33–117.

75 A. Bohm, H. Uncu and S. Komy, *Rep. Math. Phys.*, 2009, **64**, 5–32.

76 A. Bohm, *Rep. Math. Phys.*, 2011, **67**, 279–303.

77 N. Moiseyev, *Phys. Rep.*, 1998, **302**, 211–293.

78 J. Z. H. Zhang and W. H. Miller, *J. Chem. Phys.*, 1989, **91**, 1528–1547.

79 G. C. Groenenboom and D. T. Colbert, *J. Chem. Phys.*, 1993, **99**, 9681–9696.

80 G. C. Groenenboom, *J. Chem. Phys.*, 1998, **108**, 5670–5676.

81 G. C. Groenenboom, *J. Chem. Phys.*, 1998, **108**, 5677–5682.

82 J. M. Bowman, T. Carrington and H.-D. Meyer, *Mol. Phys.*, 2008, **106**, 2145–2182.

83 A. G. Császár, C. Fábri, T. Szidarovszky, E. Mátyus, T. Furtenbacher and G. Czakó, *Phys. Chem. Chem. Phys.*, 2012, **13**, 1085–1106.

84 H. S. Taylor, *Adv. Chem. Phys.*, 1970, **18**, 91–147.

85 A. U. Hazi and H. S. Taylor, *Phys. Rev. A*, 1970, **1**, 1109–1120.

86 V. A. Mandelshtam, T. R. Ravuri and H. S. Taylor, *Phys. Rev. Lett.*, 1993, **70**, 1932–1935.

87 A. Riera, *J. Phys. Chem.*, 1993, **97**, 1558–1565.

88 U. V. Riss and H. D. Meyer, *J. Phys. B*, 1993, **26**, 4503–4536.

89 J. Muga, J. Palao, B. Navarro and I. Egusquiza, *Phys. Rep.*, 2004, **395**, 357–426.

90 J. Aguilar and J. M. Combes, *Commun. Math. Phys.*, 1971, **22**, 269–279.

91 E. Balslev and J. M. Combes, *Commun. Math. Phys.*, 1971, **22**, 280–294.

92 B. Simon, *Commun. Math. Phys.*, 1972, **27**, 1–9.

93 B. Simon, *Ann. Math.*, 1973, **97**, 247–274.

94 C. van Winter, *J. Math. Anal. Appl.*, 1974, **47**, 633–670.

95 J. Simons, *Int. J. Quant. Chem.*, 1980, **14**, 113–121.

96 W. P. Reinhardt, *Ann. Rev. Phys. Chem.*, 1982, **33**, 223–255.

97 Y. K. Ho, *Phys. Rep.*, 1983, **99**, 1–68.

98 V. Mandelshtam and N. Moiseyev, *J. Chem. Phys.*, 1996, **104**, 6192–6195.

99 J. B. Kim, M. L. Weichman, T. F. Sjolander, D. M. Neumark, J. Klos, M. H. Alexander and D. E. Manolopoulos, *Science*, 2015, **349**, 510–513.

100 H. Guo, *Rev. Comput. Chem.*, 2007, **25**, 285–347.

101 T. Furtenbacher, T. Szidarovszky, J. Hrubý, A. A. Kyuberis, N. F. Zobov, O. L. Polyansky, J. Tennyson and A. G. Császár, *J. Phys. Chem. Ref. Data*, 2016, **45**, 043104.

102 I. Simkó, T. Furtenbacher, N. Dénes, T. Szidarovszky, J. Hrubý, N. F. Zobov, O. L. Polyansky, J. Tennyson and A. G. Császár, *J. Phys. Chem. Ref. Data*, 2017, **46**, 023104.

103 J. Tennyson, M. A. Kostin, P. Barletta, G. J. Harris, O. L. Polyansky, J. Ramanlal and N. F. Zobov, *Comput. Phys. Commun.*, 2004, **163**, 85–116.

104 T. Szidarovszky, A. G. Császár and G. Czakó, *Phys. Chem. Chem. Phys.*, 2010, **12**, 8373–8386.

105 A. G. Császár, E. Mátyus, T. Szidarovszky, L. Lodi, N. F. Zobov, S. V. Shirin, O. L. Polyansky and J. Tennyson, *J. Quant. Spectrosc. Radiat. Transfer*, 2010, **111**, 1043–1064.

106 A. G. Császár, C. Fábri and J. Sarka, *WIREs Comput. Mol. Sci.*, 2020, **10**, e1432.

107 C. Fábri, J. Sarka and A. G. Császár, *J. Chem. Phys.*, 2014, **140**, 051101.

108 J. Sarka, C. Fábri, T. Szidarovszky, A. G. Császár, Z. Lin and A. B. McCoy, *Mol. Phys.*, 2015, **113**, 1873–1883.

109 J. Sarka and A. G. Császár, *J. Chem. Phys.*, 2016, **144**, 154309.

110 C. Fábri, M. Quack and A. G. Császár, *J. Chem. Phys.*, 2017, **147**, 134101.

111 C. Fábri and A. G. Császár, *Phys. Chem. Chem. Phys.*, 2018, **20**, 16913–16917.

112 J. Sarka, A. G. Császár, S. C. Althorpe, D. J. Wales and E. Mátyus, *Phys. Chem. Chem. Phys.*, 2016, **18**, 22816–22826.

113 J. Sarka, A. G. Császár and E. Mátyus, *Phys. Chem. Chem. Phys.*, 2017, **19**, 15335–15345.

114 E. Bieske and O. Dopfer, *Chem. Rev.*, 2000, **100**, 3963–3998.

115 T. Salomon, M. Töpfer, P. Schreier, S. Schlemmer, H. Kohguchi, L. Surin and O. Asvany, *Phys. Chem. Chem. Phys.*, 2019, **21**, 3440–3445.

116 T. de Jongh, M. Besemer, Q. Shuai, T. Karman, A. van der Avoird, G. C. Groenenboom and S. Y. T. van de Meerakker, *Science*, 2020, to be submitted.

117 L. D. Carr, D. DeMille, R. V. Krems and J. Ye, *New Journal of Physics*, 2009, **11**, 055049.

118 R. V. Krems, W. C. Stwalley and B. Friedrich, *Cold Molecules: Theory, Experiment, Applications*, CRC Press, Boca Raton, 2009.

119 T. Köhler, K. Góral and P. S. Julienne, *Rev. Mod. Phys.*, 2006, **78**, 1311–1361.

120 J. Zirbel, K.-K. Ni, S. Ospelkaus, J. D'Incao, C. Wieman, J. Ye and D. Jin, *Phys. Rev. Lett.*, 2008, **100**, 143201.

121 A. Micheli, G. K. Brennen and P. Zoller, *Nat. Phys.*, 2006, **2**, 341–347.

122 H. P. Büchler, E. Demler, M. Lukin, A. Micheli, N. Prokof'ev, G. Pupillo and P. Zoller, *Phys. Rev. Lett.*, 2007, **98**, 060404.

123 G. Pupillo, A. Griessner, A. Micheli, M. Ortner, D. W. Wang and P. Zoller, *Phys. Rev. Lett.*, 2008, **100**, 050402.

124 B. Yan, S. A. Moses, B. Gadway, J. P. Covey, K. R. Hazzard, A. M. Rey, D. S. Jin and J. Ye, *Nature*, 2013, **501**, 521–525.

125 M. Greiner, O. Mandel, T. Esslinger, T. W. Hänsch and I. Bloch, *Nature*, 2002, **415**, 39–44.

126 O. E. Alon, A. I. Streltsov and L. S. Cederbaum, *Phys. Rev. Lett.*, 2005, **95**, 030405.

127 C. S. Chiu, G. Ji, A. Mazurenko, D. Greif and M. Greiner, *Phys. Rev. Lett.*, 2018, **120**, 243201.

128 N. Prokof'ev and B. Svistunov, *Phys. Rev. Lett.*, 2005, **94**, 155302.

129 L. Chomaz, D. Petter, P. Ilzhöfer, G. Natale, A. Trautmann, C. Politi, G. Durastante, R. M. W. van Bijnen, A. Patscheider, M. Sohmen, M. J. Mark and F. Ferlaino, *Phys. Rev. X*, 2019, **9**, 021012.

130 F. Böttcher, J.-N. Schmidt, M. Wenzel, J. Hertkorn, M. Guo, T. Langen and T. Pfau, *Phys. Rev. X*, 2019, **9**, 011051.

131 M. Morita, R. V. Krems and T. V. Tscherbul, *Phys. Rev. Lett.*, 2019, **123**, 013401.

132 J. F. E. Croft, N. Balakrishnan and B. K. Kendrick, *Phys. Rev. A*, 2017, **96**, 062707.

133 E. P. Wigner, *Annals of Mathematics*, 1951, **53**, 36–67.

134 F. J. Dyson, *J. Math. Phys.*, 1962, **3**, 140–156.

135 C. E. Porter and R. G. Thomas, *Phys. Rev.*, 1956, **104**, 483–491.

136 H. D. Simon, *Int. J. Quant. Chem.*, 1978, **14**, 529–542.

137 B. R. Junker, *Adv. At. Mol. Phys.*, 1982, **18**, 207–263.

138 J. C. Polanyi and A. H. Zewail, *Acc. Chem. Res.*, 1995, **28**, 119–132.

139 F. Fernández-Alonso and R. N. Zare, *Annu. Rev. Phys. Chem.*, 2002, **53**, 67–99.

140 The entire issue 4 of volume 14 (1978) of the *International Journal of Quantum Chemistry* was devoted to the technique of complex coordinate scaling, at that time, and occasionally even today, called "complex scaling".

141 The entire issue 5 of volume 31 (May 1987) of the *International Journal of Quantum Chemistry* was devoted to resonances.

142 *Resonances*, ed. D. G. Truhlar, American Chemical Society, 1984.

143 V. I. Kukulin, V. M. Kasnopolsky and J. Horacek, *Theory of Resonances*, Kluwer, Dordrecht, 1988.

144 *Advances in Quantum Chemistry*, ed. C. A. Nicolaides and E. Brändas, Academic Press, Oxford, 2010, vol. 60.

145 *Advances in Quantum Chemistry*, ed. C. A. Nicolaides and E. Brändas, Academic Press, Oxford, 2012, vol. 63.

146 E. Mátyus, G. Czakó and A. G. Császár, *J. Chem. Phys.*, 2009, **130**, 134112.

147 C. Fábri, E. Mátyus and A. G. Császár, *J. Chem. Phys.*, 2011, **134**, 074105.

148 J. Luque and D. R. Crosley, *J. Chem. Phys.*, 1998, **109**, 439–448.

149 M. Bixon and J. Jortner, *J. Chem. Phys.*, 1968, **48**, 715–726.

150 G. C. Schatz and M. A. Ratner, *Quantum Mechanics in Chemistry*, Dover, New York, 2002.

151 J. M. Hutson and B. J. Howard, *Mol. Phys.*, 1982, **45**, 791–805.

152 C. M. Lovejoy and D. J. Nesbitt, *J. Chem. Phys.*, 1990, **93**, 5387–5407.

153 C. M. Lovejoy and D. J. Nesbitt, *J. Chem. Phys.*, 1991, **94**, 208–223.

154 A. van der Avoird, P. E. S. Wormer and R. Moszynski, *Chem. Rev.*, 1994, **94**, 1931–1974.

155 R. Marquardt, *Mol. Phys.*, 2019, **117**, 1964–1970.

156 T. Szidarovszky and A. G. Császár, *J. Chem. Phys.*, 2015, **142**, 014103.

157 U. Fano, *Phys. Rev.*, 1961, **124**, 1866.

158 V. Brems, T. Beyer, B. M. Nestmann, H.-D. Meyer and L. S. Cederbaum, *J. Chem. Phys.*, 2002, **117**, 10635.

159 J. William A. Lester, in *The N coupled-channel problem*, ed. W. H. Miller, Plenum, New York, 1976, pp. 1–32.

160 G. C. Schatz, J. M. Bowman and A. Kuppermann, *J. Chem. Phys.*, 1975, **63**, 674–684.

161 K. Raghavachari, G. W. Trucks, J. A. Pople and M. Head-Gordon, *Chem. Phys. Lett.*, 1989, **157**, 479–483.

162 Y. J. Bomble, J. F. Stanton, M. Kállay and J. Gauss, *J. Chem. Phys.*, 2005, **123**, 054101.

163 A. van der Avoird, P. E. S. Wormer and R. Moszynski, *Chem. Rev.*, 1994, **94**, 1931–1974.

164 J. M. Hutson and S. Green, MOLSCAT computer code, version 14 (1994), distributed by Collaborative Computational Project No. 6 of the Engineering and Physical Sciences Research Council (UK).

165 The HIBRIDON package was written by M. H. Alexander, D. E. Manolopoulos, H.-J. Werner, and B. Follmeg, with contributions by P. F. Vohralik, D. Lemoine, G. Corey, R. Gordon, B. Johnson, T. Orlikowski, A. Berning, A. Degli-Esposti, C. Rist, P. Dagdigian, B. Pouilly, G. van der Sanden, M. Yang, F. de Weerd, S. Gregurick, and J. Kłos, http://www2.chem.umd.edu/groups/alexander/.

166 R. V. Krems, TwoBC - quantum scattering program, University of British Columbia, Vancouver, Canada, 2006.

167 B. R. Johnson, *J. Chem. Phys.*, 1977, **67**, 4086–4093.

168 M. H. Alexander, *J. Chem. Phys.*, 1984, **81**, 4510–4516.

169 M. H. Alexander and D. E. Manolopoulos, *J. Chem. Phys.*, 1987, **86**, 2044–2050.

170 B. R. Johnson, *J. Chem. Phys.*, 1978, **69**, 4678–4688.

171 B. R. Johnson, *NRCC Proceedings*, 1979, **5**, 86.

172 M. S. Child, *Molecular Collision Theory*, Academic, New York, 1974.

173 C. J. Ashton, M. S. Child and J. M. Hutson, *J. Chem. Phys.*, 1983, **78**, 4025–4039.

174 K. B. Gubbels, S. Y. T. van de Meerakker, G. C. Groenenboom, G. Meijer and A. van der Avoird, *J. Chem. Phys.*, 2012, **136**, 074301.

175 Q. Ma, A. van der Avoird, J. Loreau, M. H. Alexander, S. Y. T. van de Meerakker and P. J. Dagdigian, *J. Chem. Phys.*, 2015, **143**, 044312.

176 M. H. Alexander, S. Gregurick and P. J. Dagdigian, *J. Chem. Phys.*, 1994, **101**, 2887–2902.

177 M. H. Alexander and P. J. Dagdigian, *J. Chem. Phys.*, 1994, **101**, 7468–7479.

178 S. L. Holmgren, M. Waldman and W. Klemperer, *J. Chem. Phys.*, 1977, **67**, 4414–4422.

179 W. Kohn, *Phys. Rev.*, 1948, **74**, 1763–1772.

180 D. T. Colbert and W. H. Miller, *J. Chem. Phys.*, 1992, **96**, 1982–1991.

181 D. O. Harris, G. G. Engerholm and W. D. Gwinn, *J. Chem. Phys.*, 1965, **43**, 1515–1517.

182 V. Szalay, *J. Chem. Phys.*, 1993, **99**, 1978–1984.

183 H. Hellman, *Einführung in die Quantenchemie*, Franz Deuticke, Leipzig, 1937, p. 285.

184 R. P. Feynman, *Phys. Rev.*, 1939, **56**, 340–343.

185 J. Muller, X. Z. Yang and J. Burgdorfer, *Phys. Rev. A*, 1994, **49**, 2470–2475.

186 E. Mátyus, *J. Phys. Chem. A*, 2013, **117**, 7195–7206.

187 W. H. Miller, *Chem. Phys. Lett.*, 1970, **7**, 431–431.

188 G. Jolicard and E. Austin, *Chem. Phys. Lett.*, 1985, **121**, 106–110.

189 G. Jolicard and E. Austin, *Chem. Phys.*, 1986, **103**, 295–302.

190 J. G, C. Leforestier and E. J. Austin, *J. Chem. Phys.*, 1988, **88**, 1026–1031.

191 G. Jolicard and G. D. Billing, *J. Chem. Phys.*, 1992, **97**, 997–1003.

192 A. Vibók and G. G. Balint-Kurti, *J. Chem. Phys.*, 1992, **96**, 7615–7622.

193 G. J. Halász and A. Vibók, *Chem. Phys. Lett.*, 2000, **323**, 287–292.

194 B. Poirier and T. Carrington, *J. Chem. Phys.*, 2003, **119**, 77–89.

195 B. Poirier and T. Carrington, *J. Chem. Phys.*, 2003, **118**, 17–28.

196 D. Neuhasuer and M. Baer, *J. Chem. Phys.*, 1989, **90**, 4351–4355.

197 A. Vibók and G. G. Balint-Kurti, *J. Phys. Chem.*, 1992, **96**, 8712–8719.

198 Á. Vibók and G. J. Halász, *Phys. Chem. Chem. Phys.*, 2001, **3**, 3048–3051.

199 K. K. Datta and S.-I. Chu, *Chem. Phys. Lett.*, 1982, **87**, 357–364.

200 K. Museth and C. Leforestier, *J. Chem. Phys.*, 1996, **104**, 7008–7014.

201 B. Simon, *Phy. Lett. A*, 1979, **71**, 211–214.

202 J. D. Morgan and B. Simon, *J. Phys. B*, 1981, **14**, L167–L171.

203 H. O. Karlsson, *J. Chem. Phys.*, 1998, **108**, 3849–3853.

204 A. Scrinzi and N. Elander, *J. Chem. Phys.*, 1993, **98**, 3866–3875.

205 U. V. Riss and H.-D. Meyer, *J. Phys. B*, 1998, **31**, 2279–2304.

206 S. Larimian, S. Erattupuzha, E. Lötstedt, T. Szidarovszky, R. Maurer, S. Roither, M. Schöffler, D. Kartashov, A. Baltuška, K. Yamanouchi, M. Kitzler and X. Xie, *Phys. Rev. A*, 2016, **93**, 053405.

207 D. R. Herschbach, *Discuss. Faraday Soc.*, 1962, **33**, 149–161.

208 E. A. Donley, N. R. Claussen, S. T. Thompson and C. E. Wiemann, *Nature*, 2002, **417**, 529–533.

209 E. Frishman and M. Shapiro, *Phys. Rev. Lett.*, 2001, **87**, 253001.

210 A. García-Vela, *J. Phys. Chem. Lett.*, 2012, **3**, 1941–1945.

211 A. García-Vela, *Phys. Rev. Lett.*, 2018, **121**, 153204.

212 V. Zeman, M. Shapiro and P. Brumer, *Phys. Rev. Lett.*, 2004, **92**, 133204.

213 A. García-Vela and N. E. Henriksen, *The Journal of Physical Chemistry Letters*, 2015, **6**, 824–829.

214 S. Y. T. van de Meerakker, private communication.

215 T. V. Tscherbul, G. C. Groenenboom, R. V. Krems and A. Dalgarno, *Faraday Discuss.*, 2009, **142**, 127–141.

216 Z. Pavlovic, T. V. Tscherbul, H. R. Sadeghpour, G. C. Groenenboom and A. Dalgarno, *J. Phys. Chem. A*, 2009, **113**, 14670–14680.

217 L. M. C. Janssen, P. S. Żuchowski, A. van der Avoird, G. C. Groenenboom and J. M. Hutson, *Phys. Rev. A*, 2011, **83**, 022713.

218 L. M. C. Janssen, A. van der Avoird and G. C. Groenenboom, *Phys. Rev. Lett.*, 2013, **110**, 063201.